DEVELOPMENT OF EXPERIMENTAL AND NUMERICAL TOOLS FOR MAGNETIC DRUG TARGETING IN CARDIOVASCULAR FLOW

by

Ashley Kaitlin Ciero

A thesis submitted to the faculty of
The University of North Carolina at Charlotte
in partial fulfillment of the requirements
for the degree of Master of Science in
Applied Energy and Electromechanical Systems

Charlotte

2019

Approved by:

____

Dr. Rodward L. Hewlin, Jr.

____

Dr. Wesley Williams

____

Dr. Maciej Noras

ABSTRACT

ASHLEY KAITLIN CIERO. Development of Experimental and Numerical Tools for Magnetic Drug Targeting in Cardiovascular Flow. (Under the Direction of DR. RODWARD L. HEWLIN, JR.)

The aim of the present work is to design and develop experimental and numerical tools to investigate the practicality of magnetic drug targeting (MDT) in a patient-specific diseased left carotid bifurcation artery for the potential prospects of treating cardiovascular disease. MDT of therapeutic agents using multifunctional carrier particles has the potential to provide effective treatment of both cancer and cardiovascular disease by enabling a variety of localized treatment and diagnostic modalities while minimizing side effects. A computational model was developed using ANSYS FLUENT commercial software to simulate pulsatile blood flow, particle motion, and particle tracking in a diseased left carotid bifurcation artery using the magnetic properties of magnetite (Fe_3O_4) and equations describing the forces acting on particles produced by an external cylindrical electromagnetic coil. A Eulerian-Lagrangian technique is adopted to resolve the hemodynamic flow and the motion of particles under the influence of a magnetic field ($B_r = 2T$).

The computational simulations demonstrate that the greatest particle capture efficiency results for particle diameters within the micron range, specifically 4µm in regions where flow separation and vortices are at a minimum. It was also determined that the capture efficiency of particles decreases substantially with particle diameter, especially in the superparamagnetic regime. Particle diameter sizes of 20 nm- 4 μm in diameter were considered. Particles larger than 2 μm were efficiently captured at the desired location by the external magnetic field, and the largest capture efficiency observed was approximately 98%. Overall, the computational simulations indicate a substantial and promising potential for MDT as a treatment technique for cardiovascular disease. Experimental tools consisting of a phase locked particle image velocimetry system and *in vitro* cardiovascular flow loop was developed to validate flow patterns and the magnitude of drag produced by cardiovascular flow in the carotid artery for the computational simulations. The design and development techniques as well as the calibration techniques are described in detail.

ACKNOWLEDGEMENTS

I would like to acknowledge my advisor, Dr. Rodward Hewlin Jr., for all his help and allowing me to produce publish-worthy work. He has been a great advisor and I am honored to be able to work with him.

Nicholas Stanley and William Timms should also be acknowledged for all their hard work and help in creating the PIV system and the 3-D printing flow conduits.

I would like to acknowledge the North Carolina Space Grant Graduate fellowship through the National Aeronautics and Space Administration (NASA) which provided financial support during my research for the Summer of 2018.

I would also like to thank the College of Engineering at the University of North Carolina at Charlotte for the use of their equipment and lab space as well as their financial support through my last year of my degree.

Thank you to my committee members, Dr. Wesley Williams and Dr. Maciej Noras, for their support and advise.

TABLE OF CONTENTS

LIST OF TABLES

LIST OF FIGURES

CHAPTER 1: INTRODUCTION

1.1 Background

Cardiovascular disease (CVD) accounts for approximately one third of all deaths worldwide. CVDs such as coronary heart disease accounts for 1 in 7 deaths in the US, killing over 360,000 people per year (Association, 2017). The World Health Organization (WHO) states that an estimated 17.7 million people died from CVDs in 2015, representing 31% of all global deaths (Association, 2017). The estimated cost of CVD is projected to be $1,044 billion by 2030.

Current methods of treating stenosis, the narrowing of the artery, for CVD patients are bare metal stents or drug eluding stents. Bare metal stents are metal mesh tubes that are inserted into the affected area to reopen blood flow in the artery. Drug eluding stents are more efficient than bare metal stents because they release drugs to minimize rejection of the stent as well as thrombosis, the buildup of scar tissue around the stent (Kaare H. Bønaa, 2016) and is shown in *Figure 1.1 (Tuoi Vo, 2017).* With drug eluding stents, the amount of drug released is uncontrolled and long-term exposure can cause thrombosis. The use of Magnetic Drug Targeting (MDT) aims to replace or enhance the current methods of treatment for stenosis by controlling the amount of drug released in drug eluding stents.

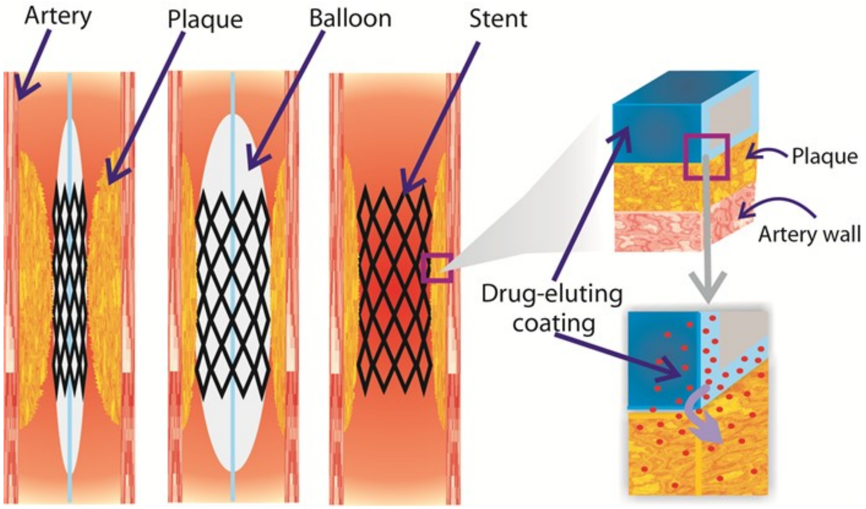

Figure 1.1: Drug Eluding Stent, obtained from (Lunnoo & Puangmali, 2015)

MDT consist of implementing and guiding drug coated Superparamagnetic Iron Oxide Nanoparticles (SPIONS) as carrier vessels for therapeutic agents to treatment sites under the influence of an external magnetic field, which is shown in *Figure 1.2 (Lunnoo & Puangmali, 2015)*. Drug coated SPIONS would be injected near the affected artery and would be directed towards the stent via a magnetic field. This would increase control over the amount of drug to the area.

There are two main concerns when considering MDT as a viable treatment for CVD. Large amounts of magnetic fields can cause negative effects on the human body, the maximum magnetic field strength cannot exceed 0.28 MA/m. (Hajiaghajani, Hashemi, & Abdolali, 2017). Since arteries have varying diameters and geometries, flow will be unsteady causing high helical vortices that will increase the difficulty of successfully targeting the SPIONS (Momeni Larimi, Ramiar, & Ranjbar, 2016).

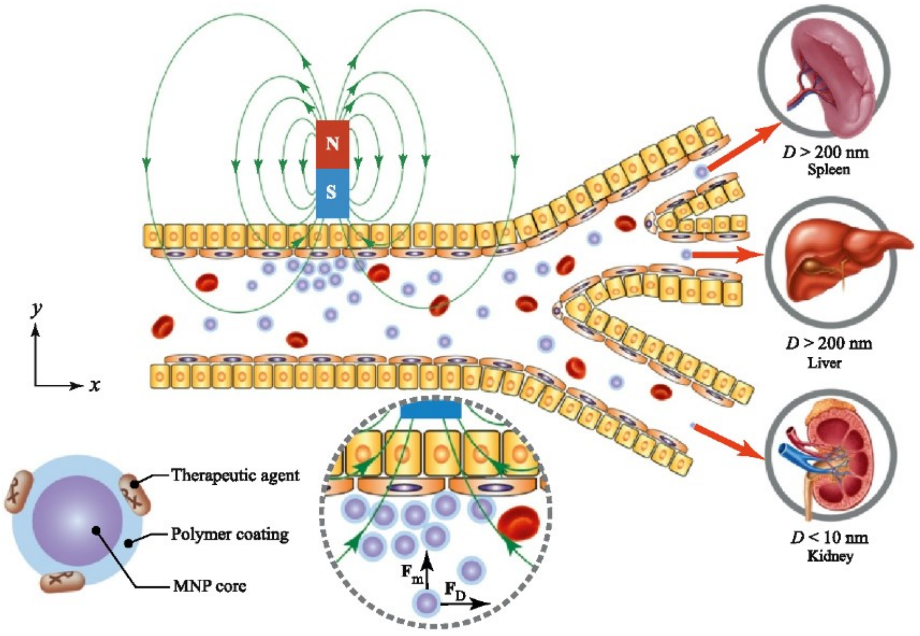

Figure 1.2: Magnetic Drug Targeting, obtained from (Hajiaghajani et al., 2017)

1.2 Problem Statement and Specific Objectives

The ultimate goal of this research is to assist in the development of measuring instruments and computational tools to verify the validity of medical drug targeting (MDT) as a potentially viable treatment technique for both cardiovascular disease and cancer. In-house measuring instruments and computational tools were developed as they are not readily available and tuned to tackle the objectives of this research.

These measuring instruments and tools consisted of: an in-house developed Phase Locked Particle Imaging Velocimetry system, a mock arterial flow loop with a customized pulsatile pump (capable of producing physiological waveforms), and a commercial computational fluid dynamic (CFD) software with added user defined function (customized add on codes to model magnetic effects). The specific objectives of my research are listed below:

1. Developed computational tools to mimic the transitional characteristics of cardiovascular flow and behavior of particles under the influence of a magnetic field. **Significance:** *The developed system was implemented to target magnetic nanoparticles via an external magnetic field. Hence, knowing the volume of particles injected into the flow stream and measuring the volume of particles present downstream of the targeting area, a targeting efficiency estimate was inferred.*
2. Designed and developed a DPIV system for analyzing pulsatile flow fields in straight rigid vessels and compliant vessels. **Significance:** *The characteristics of flow in a straight tube was indirectly and non-invasively measured via a DPIV system to create a baseline for hydrodynamic drag forces produced by the flow stream. This provided insight on the level of hydrodynamic drag forces that are present and that must be overcome to target particles via magnetic forces.*
3. Compared experimental results to numerical results. **Significance:** *Pulsatile flow were modeled in both a straight tube and an artery via commercial coding. The commercial code was also modified to include the Maxwell equations that describe the physics of an external magnetic field for MDT applications. Numerical results were compared with experimental results to validate and verify.*

CHAPTER 2: LITERATURE REVIEW

MDT is important because it can aid in cancer research and contribute to the minimizing of arterial blockages. By coating the particles in drugs to help decrease cancerous tumors, they can be injected in the arteries near the tumor and directed to the location of the cancerous cells. This will limit the side effects of the drugs since they will be centralized and not spread throughout the body (Alexiou et al., 2005) (Alexiou et al., 2011). Huang et al. ensured that the cancer fighting drug coated particles would be viable in the human body's varying pH levels (Huang, Lu, & Chen, 2017). Ravichandran et al. also looked into the pH levels of the body when studying if gold coating the particles would allow MDT to be more effective(Ravichandran et al., 2017). Some other uses for MDT include dispersing drugs more effectively for root canals or improve MRI results (Ajkidkarn, Ritprajak, Injumpa, Porntaveetus, & Insin, 2017) (Zhang, Le, & Yoon, 2017). In order to understand how magnetic nanoparticles, interact in blood, the forces and parameters in the system need to first be researched before beginning experiments.

Cherry et al. conducted a numerical simulation to monitor the forces acting on the particles in two different geometric vessels: straight pipe and bifurcating pipe. Drag forces, viscous forces, and particle interaction were the parameters that were taken into consideration in this simulation. The results of the study showed that the forces against the particles are slightly too strong to be able to have the particles remain in one location. Although the particles could not be effectively held in place, they could be directed to a certain path with the correct magnetic field strength (Cherry & Eaton, 2014). Tehrani et al. concluded that the drag forces of blood on the particles are too great to try to move particles in the complete opposite direction of the fluid. The particles should move with the flow of the fluid and the magnet could be applied to direct the particles to a specific pathway that the fluid is moving in (Tehrani, Kim, & Yoon, 2014).

Researching the effects of external magnetic forces on the system before conducting an experiment is important so that the right magnetic field strength is generated, and that the strength does not affect any of the surrounding equipment. Mondal et al. researched the effects of the Hartmann Number (Ha) on flow rate and velocity. Ha is the ratio of the amount of magnetic force applied to the viscous forces. As the Ha increases, velocity gradually decreases. This is due to the resistive Lorentz force. As the particle concentration increases, it hinders the fluid velocity. Velocity of the particles increases as the magnetic force is increased (Mondal & Shit, 2017).

After applying the magnetic forces to the system, there were three different trends that the particles seemed to follow: controlled by velocity, magnetic field strength, or boundary layer. These trends resulted in differences of magnetic field strength, the Peclet number, and the Rankin number (Nacev, Beni, Bruno, & Shapiro, 2011). The magnetic field strength heavily depends on the location of the magnet as well as the distance between the target area and the magnet. The particle size is also a major factor in MDT (Boghi, Russo, & Gori, 2017). Although the magnetic field strength gets stronger and more effective as it gets closer to the particles, it is important to consider the heat transferred from the magnet to the skin. In addition to the distance of the field, the higher the strength of the field the hotter the skin temperature can get. This is a critical parameter when considering what magnetic field strength to use on a patient (Shit & Majee, 2015).

Cao et al. suggested that using multiple, oscillating magnets could be used as an alternative to decrease the amount of heat generated at the site of magnetic field generation

(Cao, Han, & Li, 2011). Yellen et al. experimentally tried to use a different method of creating a magnetic field. One rotating magnet and one stable magnet were used in tandem with different frequencies to target the particles (Yellen et al., 2007). Agiotis et al. suggested using a MRI type system with two permanent magnets and an electromagnet with opposing poles (Agiotis et al., 2016). To ensure that the particles would be less likely to stick to the artery walls, Hoshiar et al. simulated and conducted an experiment using a magnetic field function which produces both a positive and negative magnetic pulse via electromagnetic coils (Hoshiar, Le, Ul Amin, Kim, & Yoon, 2017).

Conducting experiments are important because not all circumstances can be considered during a simulation. Gleich et al. ran a simulation where particles were injected into a blood vessel and realized that the forces against the particles in the in vitro experiment were larger than expected (Gleich et al., 2007). *In vivo* experiments are also the next step to trials on living organisms.

Busen et al. conducted an experiment because of the difficulties in accurately predicting the characteristics of the aorta (Büsen et al., 2017). Gitter et al. created their experiment with future medical applications in mind when injecting magnetic nanoparticles into a branched tube. The setup of the experiment allowed for the glass branched tube to be easily replaced with a more accurate bifurcating artery model instead of just the tube. An external magnet was applied to one of the branches to target the particles. When the magnet was turned on, some of the particles traveled through the branch. When the magnet was turned off, no particles passed through the branch (Gitter & Odenbach, 2011). These results were similar to those conducted by Hajiaghajani et al. both numerically and experimentally (Hajiaghajani et al., 2017). Janikowska et al. used a human umbilical cord to create an *ex vivo* experiment to test MDT methods. Three different magnetic field strengths were used to gather results on the effectiveness of MDT. Two of the three strengths show results of targeting the particles while one did not. This demonstrates that the field strength is a main factor in MDT (Janikowska et al., 2017). MDT is a viable method to direct particles in the artery through at least one bifurcation, but more research must be conducted in order to see if MDT is feasible in the human body or through several bifurcations.

Experimental fluid dynamics has played a vital role in investigating pulsatile blood flow characteristics *in vitro* using mock arterial vessels to provide insight into the disease condition, disease progression, and design optimization of medical stents for disease intervention (Bluestein, 1997; Gates, 2018; Ha, 2014; Hewlin, 2018; McGloughlin, 2010; Mokhtar, 2017; Shintani, 2018). *In-vitro* studies use a physical representation of a diseased or stented artery with the goal of obtaining hemodynamic parametric data (Doyle, 2010). Particle image velocimetry (PIV) has been used extensively as a tool in *in vitro* studies to non-invasively obtain hemodynamic parametric data for diseased artery cases and stented artery cases. However, one of the key limitations involving this approach is the need to produce quality images to resolve the flow characteristics of the artery being analyzed. Some of the causes of poor image quality are due to laser glare and scattering light from the mock arterial vessel, inappropriate IOR matching of the working fluid to the vessel material, and artery models that lack optical transparency.

There are many methods for manufacturing mock arterial vessels for PIV analyses. The most common approach involves fabricating the mock artery model with a silicone elastomer using a lost casting technique (Nguyen, 2004; Stoiber, 2013; Yip, 2004). This process is very time laborious, often suffers poor transparency due to voids formed in the material during casting under vacuum and requires casting a mold in addition to a transparency box to house the artery and be filled with a fluid to achieve the same IOR as the artery material (Allard, 2009). Recent advances in *in vitro* arterial flow analysis using lost casting fabrication techniques of complex optically transparent arterial vessels have minimized some of the limitations mentioned.

In some cases, distortions due to IOR mismatch have been accounted for using image correction and/or dewarping techniques. Performing these techniques is often difficult for basic models and impossible for complex arterial models with varying diameter and branching. IOR matching is often a preferred method to avoid time consuming code development for image correction and added accessories to the PIV camera (Song, 2014). As a result, *in vitro* experiments may be conducted with inexpensive in-house developed working fluid mixtures such as distilled water and glycerol (Hopkins, 2000; Yousif, 2009).

Although few studies have been reported, some studies have reported that 3-D printing may be used to fabricate optically clear vessels suitable for PIV analyses (Lai, 2009). These studies have reported that optimal transparency is best normal to the print layering plane and poor in the direction of print layering.

Table 2.1: Overview of Previous Experimental and Numerical MDT Studies

Author	Goal	Observations	Conclusions
1.(Najjari & Plesniak, 2018)	Gather data about wall shear stress and the effects of torsion in curved pipe geometries. Find the effects of torsion on flow patterns.	Curves in the pipe resulted in an up or down motion near the wall causing vortices.	* Even small changes in the pipe, whether geometry or defects, greatly affect the flow and increase vortices.
2.(Momeni Larimi et al., 2016)	To fully understand magnetic drug targeting, the presence of a magnetic field in the carotid artery was first studied numerically in OpenFOAM.	When applying a magnetic field to the second branch of the artery, it drove the particles into the subbranch. Without this field, no particles entered the subbranch.	*The magnetic field strength used was 2T and was very effective in targeting particles 0.5 um in diameter.
3.(Janikowska et al., 2017)	To gather data about the efficiency of MDT in an *ex vivo* umbilical artery with different types of SPIONS.	Type 1, lauric acid shell, was the most effective type of SPION for MDT. Type 2, lauric acid and albumin shell, was a close second. Type 3, dextran coated shell, was not an effective coating.	*The magnet was 5mm from the artery and MDT was successful. This method could be applied to magnetized stents.
4.(Hajiaghajani et al., 2017)	A low intensity magnetic field was designed to test the efficiency of MDT in a Y shaped modeled vessel. The experiment was first conducted using numerical methods and tested in real life to compare and validate the results.	The in vitro results reported an average successful percentage of 80.2%.	*The study was simplified by neglecting the diffusive force and instead using an effective radius of particle clusters. *The maximum magnetic field strength without side effects should be 0.28 MA/m.

CHAPTER 3: METHODS AND MATERIALS

3.1 Numerical Setup and Simulation

3.1.1 Governing Equations

Particle Force Balance

The physics describing the transport of magnetic nanoparticles in the cardiovascular system is governed by various factors: (1) the magnetic force produced by the external magnet, (2) viscous drag, (3) unsteady effects due to the driving pressure wave, (4) particle kinematics *(Brownian motion)*, and (5) the interaction between the fluid and particles. In the present work, our model incorporates the dominant magnetic and viscous forces and the particle/blood interaction through an integrated force balance. This is done via deriving the magnetic force exerted on a cluster *(parcel)* of particles. Each particle has a radius R_{mp} and a spherical volume V_{mp}. The force exerted on the particles is derived from a dipole moment approach in which the particle is replaced by an equivalent point dipole which is focused at the center. The force is computed on a parcel of particles in a non-conducting medium described as:

$$F_m = \frac{4}{3}\pi R_{mp}{}^3 \mu_0 \frac{3\chi_{mp}}{(\chi_{mp}+3)}\left(H \cdot \nabla\right) H \qquad [1]$$

where H is the applied magnetic field intensity at the center of the parcel, χ_{mp} is the magnetic susceptibility (3.1) and μ_0 ($4\pi\times10^{-7}$ N·A^{-2}) is the permeability in air (Furlani, 2007). The derivation of the magnetic force incorporates the assumption that blood is a non-magnetic medium with permeability. The magnetic field in the present work is modelled as a cylindrical electromagnet of radius R_{mag} that is positioned a distance d

orthogonal to the axial flow field as shown in *Figure 3.6*. The magnetic field is described as:

$$H_x(x,y) = \frac{M_s {R_{mag}}^2}{2}\left(\frac{(x+d)^2 - y^2}{\left((x+d)^2 + y^2\right)^2}\right) \tag{2}$$

and

$$H_y(x,y) = \frac{M_s {R_{mag}}^2}{2}\left(\frac{2(x+d)y}{\left((x+d)^2 + y^2\right)^2}\right) \tag{3}$$

Equations [2] and [3] are substituted into equation [1] to determine the magnetic force components as described below in equations [4] and [5]:

$$F_{mx}(x,y) = \frac{4}{3}\pi {R_{mp}}^3 \mu_0 \frac{3\chi_{mp}}{(\chi_{mp}+3)} \times \left[H_x(x,y)\frac{\partial H_x(x,y)}{\partial x} + H_x(x,y)\frac{\partial H_x(x,y)}{\partial y} \right] \tag{4}$$

and

$$F_{my}(x,y) = \frac{4}{3}\pi {R_{mp}}^3 \mu_0 \frac{3\chi_{mp}}{(\chi_{mp}+3)} \times \left[H_y(x,y)\frac{\partial H_y(x,y)}{\partial x} + H_y(x,y)\frac{\partial H_y(x,y)}{\partial y} \right] \tag{5}$$

Equations [4] and [5] may be simplified via the differential product rule to yield the following magnetic field force components:

$$F_{mx} = \frac{-3\pi\mu_0 {R_{mp}}^3 \chi_{mp} {M_s}^2 {R_{mag}}^4}{\chi_{mp}+3} \frac{(x+d)}{2\left((x+d)^2 + y^2\right)^3} \tag{6}$$

and

$$F_{my} = -\frac{3\pi\mu_0 {R_{mp}}^3 \chi_{mp} {M_s}^2 {R_{mag}}^4}{\chi_{mp}+3} \frac{y}{2\left((x+d)^2 + y^2\right)^3} \tag{7}$$

Particle Trajectory Model

A discrete phase model (DPM) was implemented in the present work. This approach follows the Euler-Lagrange approach. The interaction with continuous phase option was enabled in Fluent to allow the discrete phase (particles) to exchange mass, momentum, and/or energy with the continuous phase (blood). The trajectory of the particles is predicted by integrating the force balance on the particle cluster, which is written in a Lagrangian reference frame. The force balance equates the particle cluster inertia with the forces acting on the particles and can be expressed as:

$$\frac{du_p}{dt} = F_D(u-u_p) + \frac{g_x\left(\rho_p-\rho\right)}{\rho_p} + F_{bi} + F_x \tag{8}$$

where u is the fluid velocity, u_p is the particle parcel velocity, ρ is the fluid density, ρ_p is the particle density, F_{bi} is the Brownian force acceleration term, F_x is the body force acceleration term, d_p is the particle diameter, and $F_D(u-u_p)$ is the drag force per unit mass and is written as:

$$F_D = \frac{18\mu}{\rho_p {d_p}^2}\frac{C_D \operatorname{Re}}{24} \tag{9}$$

The relative Reynolds number, "Re" is defined as:

$$\operatorname{Re} = \frac{\rho d_p \left|u_p - u\right|}{\mu} \tag{10}$$

the drag coefficient, "C_D" is defined as:

$$C_D = a_1 + \frac{{a_2}^2}{\operatorname{Re}} + \frac{{a_3}^3}{\operatorname{Re}^2} \tag{11}$$

where a_1, a_2, and a_3 are constants that apply for smooth particles using the spherical drag law and apply over a range of Reynolds numbers as reported by Morsi and Alexander

(Morsi, 1972). For the present work, when substituting the appropriate constants, the drag coefficient takes the following form for micron sized particles:

$$C_D = \frac{24}{\mathrm{Re}}\left(1 + b_1 \mathrm{Re}^{b_2}\right) + \frac{b_3 \mathrm{Re}}{b_4 + \mathrm{Re}} \qquad [12]$$

where:

$$\begin{gathered} b_1 = \exp(2.3288 - 6.4581\phi + 2.4486\phi^2) \\ b_2 = 0.0964 + 0.5565\phi \\ b_3 = \exp(4.905 - 13.8944\phi + 18.4222\phi^2 - 10.2599\phi^3) \\ b_4 = \exp(1.4681 + 12.2584\phi - 20.7322\phi^2 + 15.8855\phi^3) \end{gathered}$$

which is adapted from Haider and Levenspeil (Haider, 1989). The shape factor, "ϕ" is defined as:

$$\phi = \frac{s}{S} \qquad [12]$$

where *s* is the surface area of a sphere having the same volume as the particle, and *S* is the actual area of the particle. The shape factor cannot exceed a value of 1. For superparamagnetic particles, a form of Stokes drag law is used (Ounis, 1991). In this case, the drag force on a particle per unit mass is defined as:

$$F_D = \frac{18\mu}{d_p^{\,2} \rho_p C_e} \qquad [13]$$

where the Cunningham correction factor C_e is described as:

$$C_e = 1 + \frac{2\lambda}{d_p}\left(1.257 + 0.4e^{-(1.1 d_p / 2\lambda)}\right) \qquad [14]$$

and λ is the molecular mean free path. For superparamagnetic particles, the effects of Brownian motion are included. The components of the Brownian force are modeled as a Gaussian white noise process with spectral density given by $S_{n,ij}$.

$$S_{n,ij} = S_0 \delta_{ij} \quad [15]$$

where δ_{ij} is the Kronecker delta function and modelled as:

$$S_0 = \frac{216 \nu k_B T}{\pi^2 \rho d_p^{\,5} \left(\frac{\rho_p}{\rho} \right) C_e} \quad [16]$$

T is the absolute temperature of the fluid *(taken as body temperature)*, ν is the kinematic viscosity, and k_B is the Boltzmann constant. The Brownian force per unit mass component is described as:

$$F_{bi} = \zeta_i \sqrt{\frac{\pi S_0}{\Delta t}} \quad [17]$$

where ζ_i is the zero-mean unit-variance-independent Gaussian random number.

Numerical Methods

The pulsatile flow of blood and particle tracking was calculated via ANSYS Fluent™ through the use of the Continuity and Navier Stokes Equations.

$$\nabla \cdot u = 0 \quad [18]$$

$$\frac{\partial u}{\partial t} + u \cdot \nabla u = -\nabla P + \nabla \left(\mu \nabla u \right) \quad [19]$$

where u is the fluid velocity, and ρ is the fluid density.

The magnitude of the magnetic force components is substituted into the accelerated body force term in Eqn. [7]. User defined functions were written for the pulsatile velocity waveform and the magnetic force generated by the magnetic field. The user defined functions were compiled in the ANSYS Fluent platform for simultaneous flow and particle trajectory calculations. The Navier Stokes equations were solved implicitly using a quadratic upwind discretization scheme (QUICK) for nonlinear terms. The integrated force balance described in Eqn. [7] was numerically integrated using a sixth order Runge-Kutta scheme for instances where the left side of the equation was significant, and a Euler scheme otherwise. A two-way fluid-particle coupling method is implemented in Fluent to predict the effect of the discrete phase on the continuum. This method solves the discrete and continuous phase equations until the solutions of both phases have stopped changing.

The flow domain was discretized into a large number of tetrahedral computational cells. The arterial model was tested for three different mesh grid densities, i.e., 274, 548, and 835 cells in the cross-sectional flow area. The time-averaged absolute difference in centerline axial velocity between the coarse and fine cross-sectional mesh was 2.2 mm/s, and that between fine and finer one was only 1 mm/s, which was very small relative to the mean centerline axial velocity value of 105 mm/s.

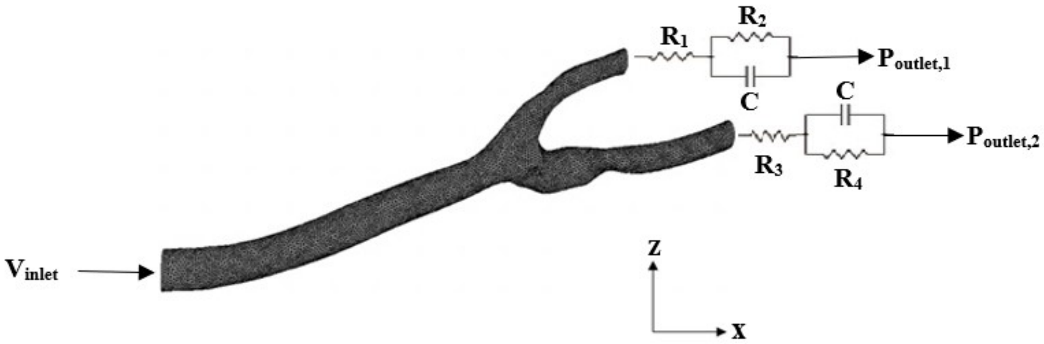

Figure 3.1: Top View of the Arterial Computational Mesh

The mesh scheme that contained 548 cells per cross-section, i.e., 230,608 for the whole arterial mesh as shown in *Figure 3.1* and evaluated over 80 timesteps per cycle provided the best grid result for independency and stability in solutions within a satisfactory CPU time.

Table 3.1: Resistance and Capacitance Values Used for the Windkessel Boundary Conditions, obtained from (Gharahi, 2016)

	R_d (Pa s/m^3)	C (m^3 /Pa)
ICA	1.11 X 10^6	4.20 X10 $^{-13}$
ECA	2.27 X 10^6	2.27 X 10 $^{-13}$

3.1.2 Geometry and Meshing

Ansys Fluent 18.2 commercial CFD software solves the Navier Stokes equations over a finite volume domain was used to analyze flow fields in both a straight pipe and patient specific bifurcating artery. The artery was from a deceased 60-year-old male with the cause of death being atherosclerosis, narrowing of the artery, from Charite' Clinical Research Hospital in Berlin, Germany. The artery was converted from a point cloud file format to a solid model via Solidworks 2016.

Three components of Ansys Fluent were used: Mesh, Fluent, CFD Post. The straight pipe, used for reference as shown in *Appendix A: Ansys Fluent Straight Pipe*, and patient specific artery were imported into the meshing component of Ansys Fluent. Virtual topologies were created to simplify the geometry by merging the surfaces. Named selections were then created to label the geometries, as shown in *Figure 3.2.*

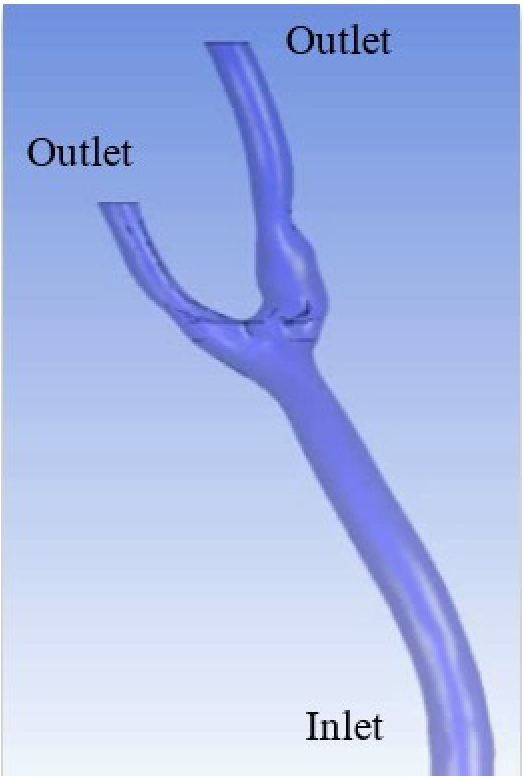

Figure 3.2: Ansys Fluent Named Selections: Artery

When using Ansys Fluent, the models represent the rigid fluid core of the geometries. The minimum cell size and inflation parameters were adjusted in the arterial model to have a more uniform mesh to increase accuracy, decrease dense mesh regions, and decrease outliers, as shown in *Figure 3.3 (a), and (b)*. The number of elements for the arterial model was 265,029 with a minimum element size of 5 x 10^{-4}.

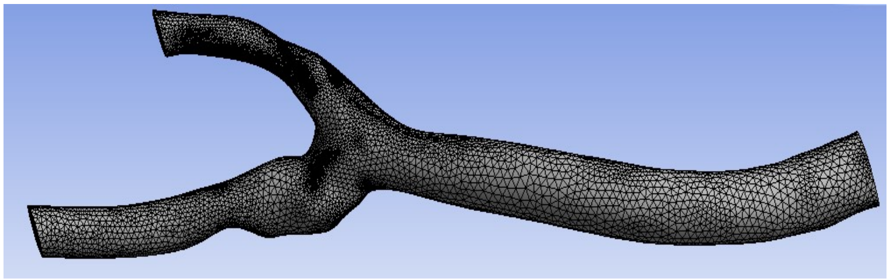

(a)

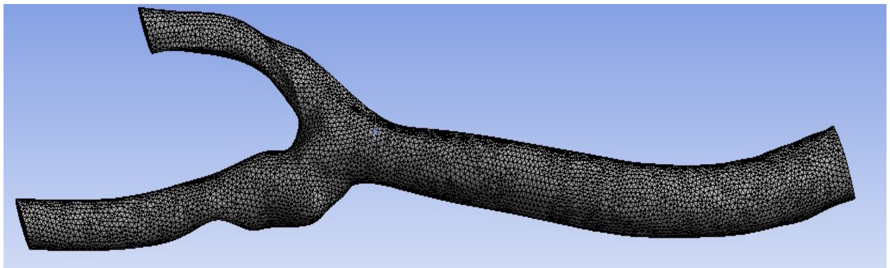

(b)

Figure 3.3: Inflation: (a) Before Inflation and (b) After Inflation

3.1.3 Working Fluid

Blood was the simulated working fluid and the Carreau model for viscosity was utilized. The parameters were chosen due to the relatively high shear rates in the carotid artery, blood is a non-Newtonian fluid, and what was used in previous research with the parameters shown in *Table 3.2 (Jiang, 2016).*

Table 3.2: Working Fluid Parameters, obtained from (Jiang, 2016)

Parameter		Unit
Density	1060	kg/m^3
Time Constant	3.313	s
Power-Law Index	0.3568	-
Zero Shear Viscosity	0.056	kg/ms
Infinite Shear Viscosity	0.0035	kg/ms
Outlet Pressures	13,332	Pa

3.1.4 Inlet Velocity

User Defined Function, UDF, subroutines were integrated into Fluent because it does not have the capabilities to have a varying inlet velocity. A UDF was created to mimic the pulsatile flow of blood in the artery at the inlet via piecewise functions. The UDF modeled 3 pulses of 0.8 seconds each with a maximum velocity of 0.43 m/s, 0.11 m/s, frequency of 1.25 Hz, and a heart rate of 75 bpm (Lockhart et al., 2006). *Figure 3.4* shows the velocity waveform that was created.

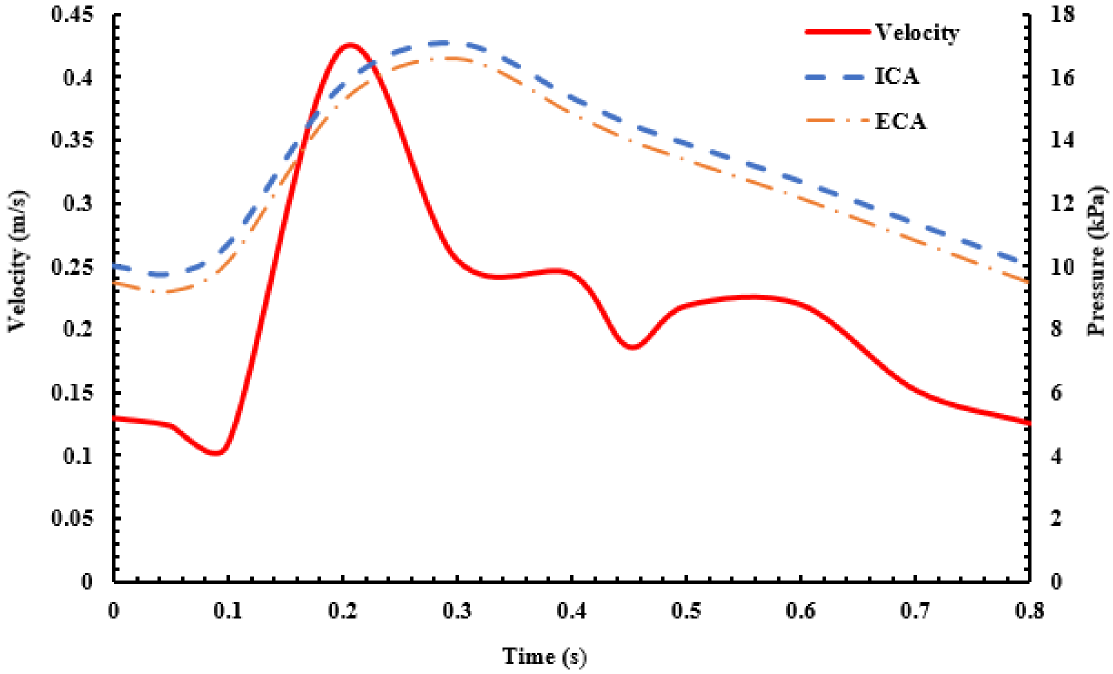

Figure 3.4: Plot of the Patient-Specific Inlet Waveform and Windkessel Outlet Waveforms

$$\bar{u}(t) = \begin{cases} 83.33t^3 - 12.50t^2 + 0.21667t + 0.13 \\ 7517.12t^4 - 5688.27t^3 + 1529.70t^2 - 169.61t + 6.6462 \\ -96.923t^3 + 100.30t^2 - 34.425t + 4.1629 \\ 58.291t^2 - 5235.7t + 1193 \\ 18.835t^3 - 36.960t^2 + 23.427t - 4.60 \end{cases} \qquad [20]$$

$$\begin{array}{l} 0s \le t \le 0.15s \\ 0.15s \le t \le 0.24s \\ 0.24s \le t \le 0.42s \\ 0.42s \le t \le 0.47s \\ 0.47s \le t < 0.80s \end{array}$$

$$u(y,t) = 2\bar{u}(t)\left[1 - \left(\frac{y}{R}\right)^2\right] \qquad [21]$$

3.1.5 Particle Injection

The corresponding flow rate of particles at the injection site was found to keep the simulation from becoming unstable. Particles were injected at the inlet of both the straight pipe and the carotid artery at rates shown in *Table 3.3.*

Table 3.3: Particle Properties

	Pipe	Artery
Injection Time	0.0 to 0.005 s	0.0 to 0.8 s
Flow Rate	$1e^{-20}$ kg/s	$1e^{-7}$ kg/s
Min Diameter	100 nm	100 nm
Max Diameter	300 nm	4000 nm
Mean Diameter	120 nm	350 nm

3.1.6 Magnet

A UDF was written to simulate a magnetohudrodynamic solver in Ansys Fluent. A magnetic field was simulated to represent the magnetic pull on the particles in fluid flow. The magnetic field strength must be below 0.28 MA/m to limit side effects on the human body (Hajiaghajani et al., 2017). The UDF does not model blood as a magnetic fluid because of the limited magnetic strength. A UDF was also developed to view the magnetic forces on the system and is shown in *Figure 3.5.* As the distance from the target area increases, the magnetic forces decay. It is suggested in literature that the magnet be 0.024 m from the affected area and at a 2T (Momeni Larimi et al., 2016), as shown in *Figure 3.6*.

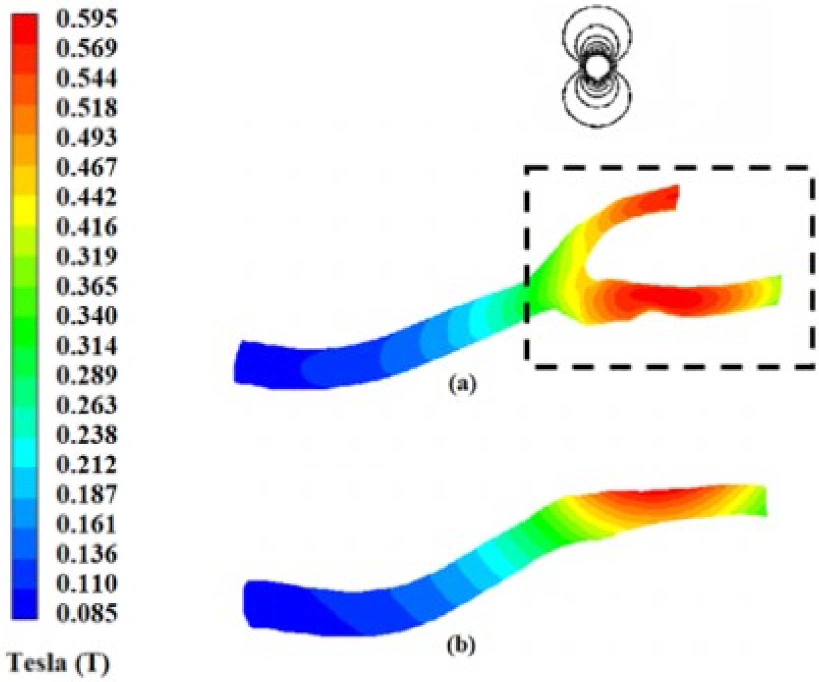

Figure 3.5: Contour of Magnetic Field Forces

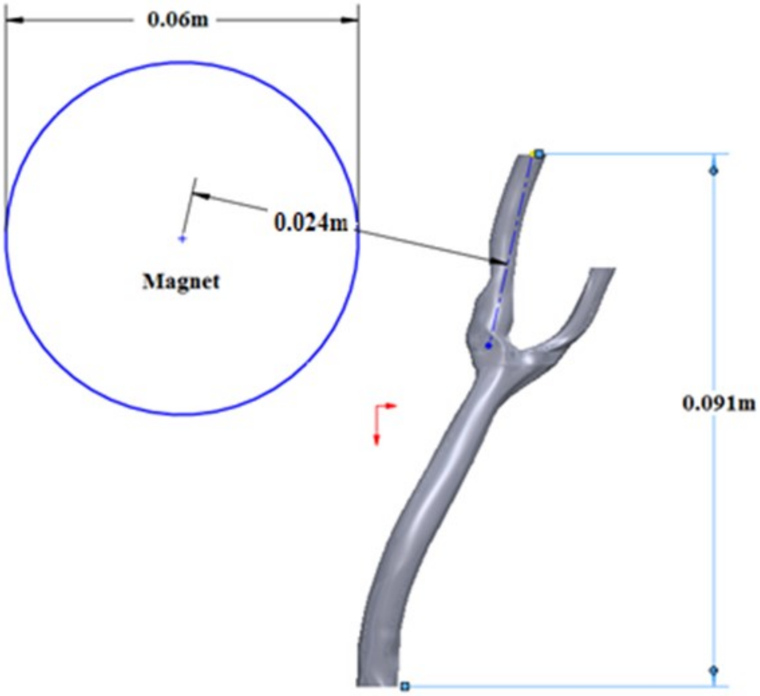

Figure 3.6: Schematic Representation of the Circular Electromagnet of Radius “R_{mag}” Distanced *“d”* from the Centerline

3.1.7 Particle Capture Efficiency

One of the most reported challenges for MDT is the capability of targeting and capturing particles via producing a magnetic force to overcome the drag force acting on particles due to the inlet pressure wave. As a result, capture efficiency is a major parameter of interest in the present work. Capture efficiency describes the effectiveness of targeting particles under the influence of a magnetic field. The capture efficiency for the magnetized section of the artery is defined as the ratio of the number of injected particle parcels to the number of particle parcels leaving the magnetized region:

$$\eta_c = \frac{N_{np,in}}{N_{np,out}} \times 100\% \qquad [22]$$

In the present work, Eqn. [17] is evaluated via imposing a reflective boundary condition at the wall of the magnetized section *(region of interest (ROI))*. Previous studies that have utilized a trapped boundary condition as opposed to a reflective boundary condition (Bose, 2014). A trapped boundary condition cancels the trajectory mapping of particle trajectories as opposed to continuously monitoring the trajectory if the particles move from the current position in a future time step. Additionally, an escape boundary condition is imposed at the outlets which allowed particles to escape *(exit)* the outlets. The capture efficiency is determined via comparing the number of injected particle parcels $N_{np,in}$ to the number of escaped particle parcels $N_{np,out}$ as described in Eqn. [22].

3.2 Experimental Setup

3.2.1 Components

The following components were used to design and develop a DPIV system to meet the specific needs of the research (Najjari & Plesniak, 2018):

- Nd:YAG Solo III pulsed Laser (New Wave Research)
- LaVision laser optic with f=-10 and f=20mm focal lens
- Flare 12MP high speed CMOS camera
- Nikon AF Micro-Nikkor 60mm f/2.8D lens
- Edmund Optics long pass filter (575nm threshold limit)
- DVR Express core 2

3.2.2 Flow Conduits

Test Sample Model

In the efforts of evaluating the practicality of using 3-D printed anatomical vessels for PIV analyses, an initial square extrusion test sample incorporating a hollow circular conduit for fluid and particle tracer flow is shown below in *Figure 3.7 (Kenneth Aycock, 2017)*.

The test sample was developed in Solidworks CAD software. The test sample was printed using a desktop Formlabs Form 2 3-D printer and stock clear resin (RS-F2-GPCL-04). The test samples were printed in a 45-degree build plane orientation as shown in *Figure 3.8.* The cube face edges are bolded in black to outline the geometry provides an illustration of the square extrusion modelled with the support material in slicer software prior to 3-D printing. For 3-D printing, the print settings were set to the finest print resolution setting, resulting in a print layer resolution of 25µm (0.001in).

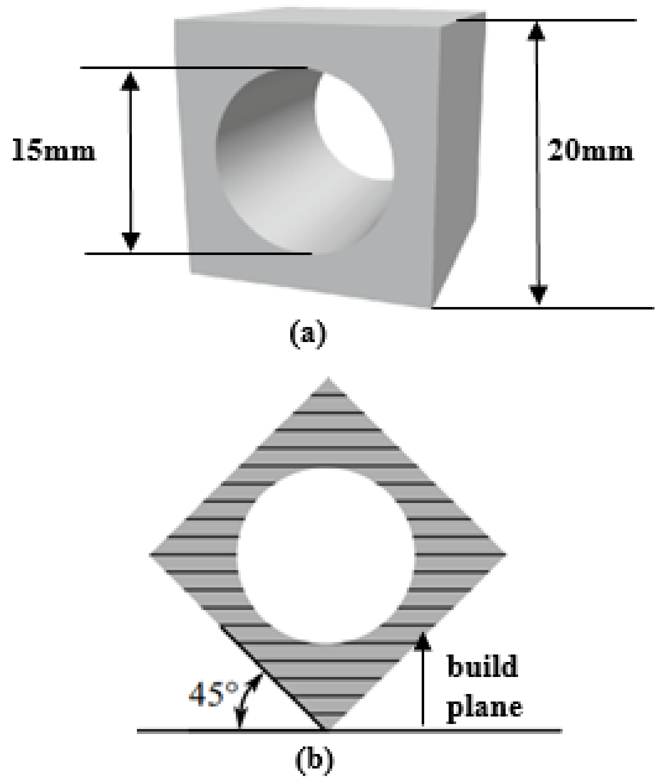

Figure 3.7: CAD Model of 3-D Printed Test Models (a) Isometric View (b) Front View Positioned 90 Degrees from the Build Plane and 45 Degrees from the Build Plane, obtained and modified from (Kenneth Aycock, 2017)

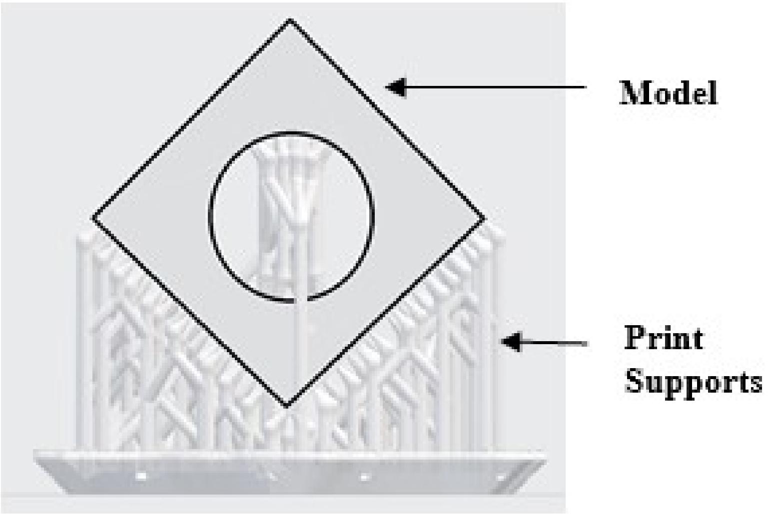

Figure 3.8: Slicer Model of Test Sample in a 45 Degree Orientation with Print Supports

The print support material was removed and then the test subject was soaked in an isopropyl alcohol solution for 20 minutes to remove additional undesired resin. Additional post processing was then done in the following steps:

1. The test sample was first placed on a motorized rotary apparatus and exposed to an ultraviolet (UV) light source to cure the resin over a 24-hour period.
2. The outer surface of the test samples was then wet-sanded perpendicular to the print layers with coarse grit sandpaper and incrementally progressing to finer grit sandpaper (P600-P2000).
3. Each surface was sanded for approximately 30 min. A honing tool was used to sand the flow conduit. Sanding was timed to improve the uniformity of resin material removal.
4. Each surface was inspected under a bright light source between and after sanding steps. Sanding of each surface was repeated for an additional 30 minutes until layering or surface defects from the previous sanding pass were no longer visible. The total sanding time was 1 hour.
5. Finally, the surfaces were polished with a micro cloth and a three-step polishing compound *(NOVUS Plastic Polish; Novus Inc., St. Paul, MN)* to obtain a transparent finish (NOVUS, 2011).

Arterial Model

To demonstrate the feasibility of fabricating a more complex 3-D printed model for PIV, we consider the patient-specific carotid bifurcation model used in our previous studies (Rodward Hewlin Jr., 2019). In preparation for 3-D printing, a negative of the carotid artery lumen was designed in Solidworks. The negative consisted of a rectangular cross section encompassing the vessel segments as shown in *Figure 3.9*. The anatomical model was fabricated following the same procedure as outlined for the test section printed part. The entire model was printed in a 45 degree build plane orientation as shown in *Figure 3.9 (b)*. The exterior of the arterial model was sanded and polished using the same steps as outlined previously. The interior of the model was not post processed and there were no interior supports that needed to be removed.

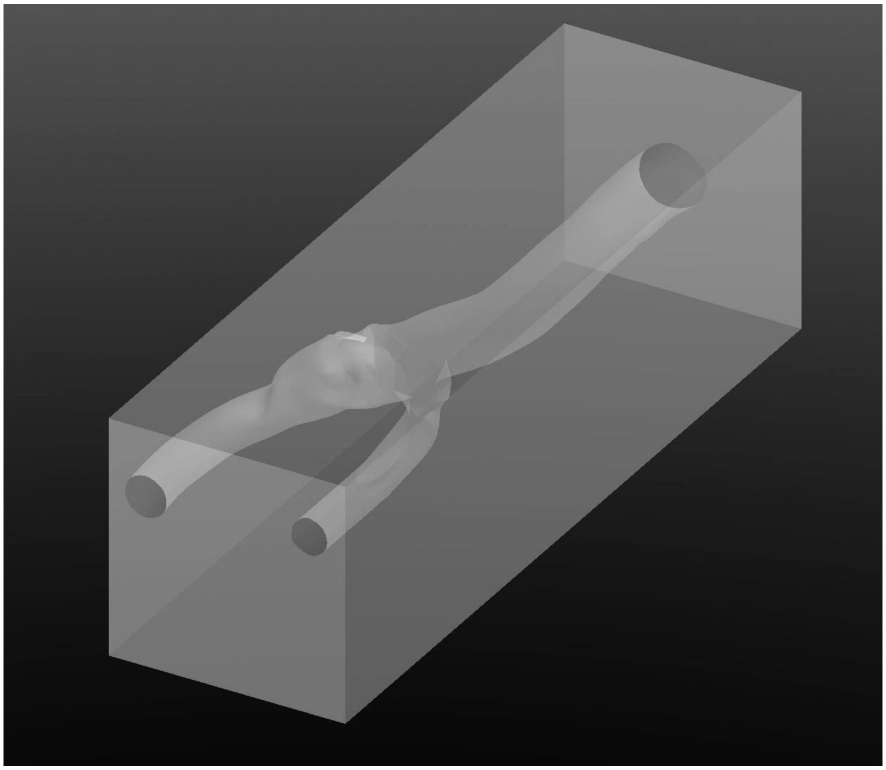

(a)

Figure 3.9: Carotid Artery Anatomical: (a) CAD Model and (b) Slicer Model with Print Supports

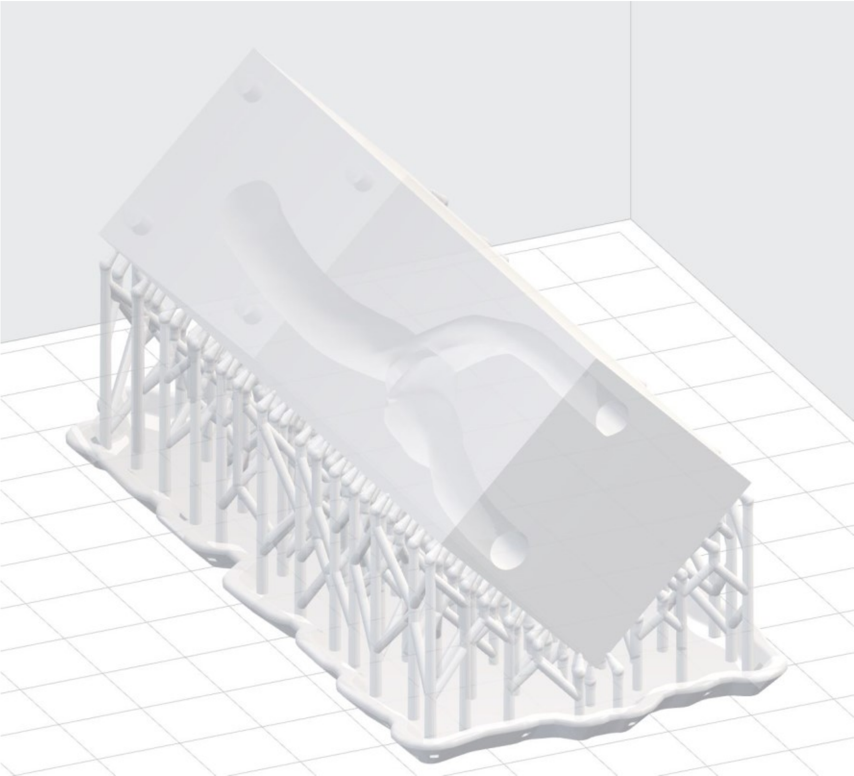

(b)

Figure 3.9, Continued

It is worth mentioning that several characteristics of the arterial model in the present work complicate traditional fabrication approaches (e.g., using computer numerical controlled [CNC] milling): (1) both the ICA and ECA branches are curved in the anteroposterior direction, and (2) the vessel cross sections are constantly varying in diameter along the centerline axis. Tradition fabrication techniques such as CNC would involve fabricating the model out of acrylic and would also require splitting the model into two sections to machine the internal surface of the lumen and then fusing the two sections together. The mate seam created by this procedure would produce issues such as restricting the laser light sheet and camera access for PIV raw image capture. Additionally, because of the varying curvature of the carotid arterial model, a four-axis CNC mill would be required to accurately reproduce the model geometry, greatly increasing the cost of fabrication. The direct 3-D printing approach presented in the present work overcomes these limitations.

3.2.3 PIV Analysis

For PIV analyses, the test sample was illuminated by a 1.0mm thick laser light sheet provided by a pulse Nd:YAG Solo III Laser by New Wave Research outfitted with a laser optic and focal lens. The test sample was filled with a working fluid composed of 53% sodium iodide (NaI), 26% glycerol, 21% distilled water, and less than 0.5% by mass of sodium thiosulfate to reduce the coloration of the fluid, mixture to match the IOR of the Formlabs stock clear resin *(IOR was reported to be 1.5304 (Formlabs, 2018) (Kenneth Aycock, 2017).*

Fluorescent polymer microspheres (Fluoro-Max 36-3B; Thermo Scientific Inc., Fremont CA) were added to the fluid to serve as tracer particles. Images were recorded with a Flare 12MP high speed CMOS camera outfitted with a Nikkon AF Micro-Nikkor 60mm f/2.8D objective and long pass filter with a 575nm threshold limit (Edmund Optics). A 1TB DVR core (DVR Express Core 2) was used to store raw tracer particle flow images. Tracer particle flow images were resolved using OPENPIV, an open source MATLAB-based PIV software. The PIV system was calibrated using a simple gravity driven flow system setup with an elevated tank open to atmosphere supplying working fluid through the piping to the test section sample. The fluid exited the system through a restricted orifice and flowed into a beaker. 3-D Printed extensions were added to the test sample to provide a sufficient entrance length and exit. A CAD model schematic is shown in *Figure 3.10.*

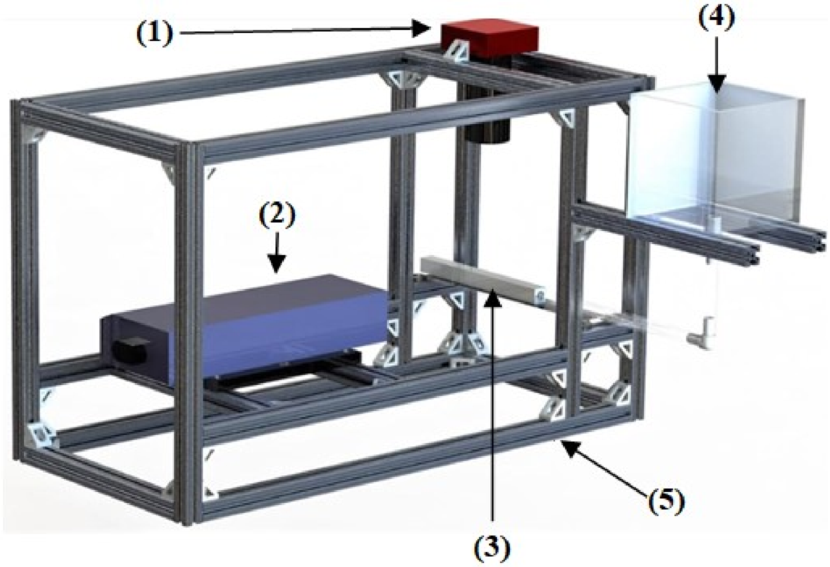

Figure 3.10 CAD of PIV System and Gravity Driven Flow System Setup: (1) Camera, (2) Laser, (3) Test Section, (4) Tank, and (5) Aluminum Framing

The fluid volumetric level was monitored and timed with a stop watch to obtain the average volumetric flow rate. The average velocity was calculated and used to obtain the theoretical velocity profile using the Poiseulli equation shown below in equation [23]:

$$u(r) = u_{avg}\left(1 - \left(\frac{r}{R}\right)^2\right) \qquad [23]$$

where u_{avg} is the average velocity, r is the radius, and R is the maximum radius. During calibration, the PIV image resolution was determined to be approximately 32 μm per pixel. The images were captured using an in-house frame straddling technique, in which a signal generator created a 15 Hz square wave that fired the camera shutter. The camera was set to capture images in double exposure and set to 30 frames per second with a first frame exposure of 500 μs in order to sync with the laser pulses. A dual pulse laser would fire based on the generated square wave at a delay of 250 μs and 750 μs for the first and second laser respectively. The Q-switch was then set to a delay of 192 microseconds for each laser pulse as instructed for best results (Nicholas Stanley, 2019) (Research, 2006). This setup produced approximately 250 image pairs in a 16.7 s recording with a timestamp of 66.7 ms between each image pair and 500 µs between the images in the pair.

To demonstrate that the model is suitable for transient flows, a simple flow loop was assembled from plastic tubing, barbed fittings, a custom pulsatile pump (BDC Labs model PD-1100 Wheat Ridge, CO), and a DAQ system to circulate flow from the compliance chamber to the test section. A sinusoidal volumetric waveform was implemented at the inlet with a peak volumetric magnitude of 1 L/min at a frequency of 60 beats/min, as shown in *Figure 3.12 (a) PIV System with Pulsatile Pump and Compliance Chamber*, *Figure 3.12 (b) Pulsatile Pump and Compliance Chamber,* and *Figure 3.11.*

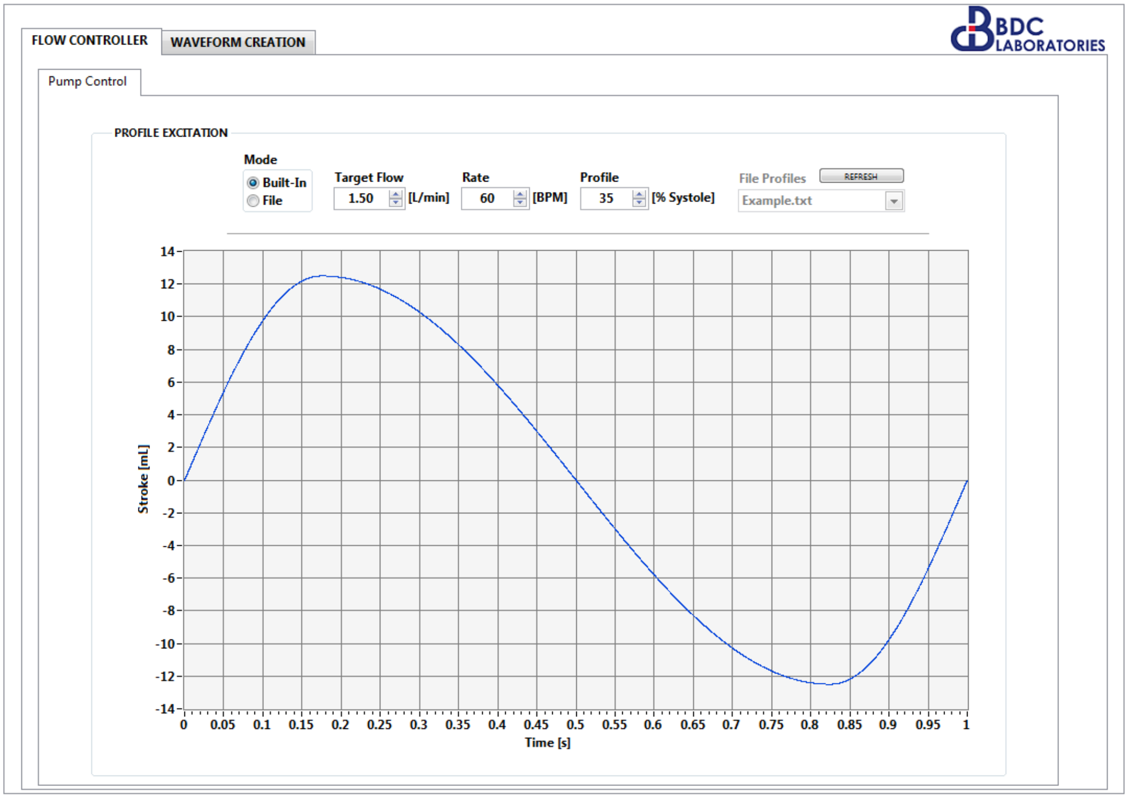

Mode
● Built-In
○ File

Target Flow 1.50 [L/min]

Rate 60 [BPM]

Profile 35 [% Systole]

File Profiles Example.txt

Figure 3.11: Pulsatile Pump Sine Wave Example

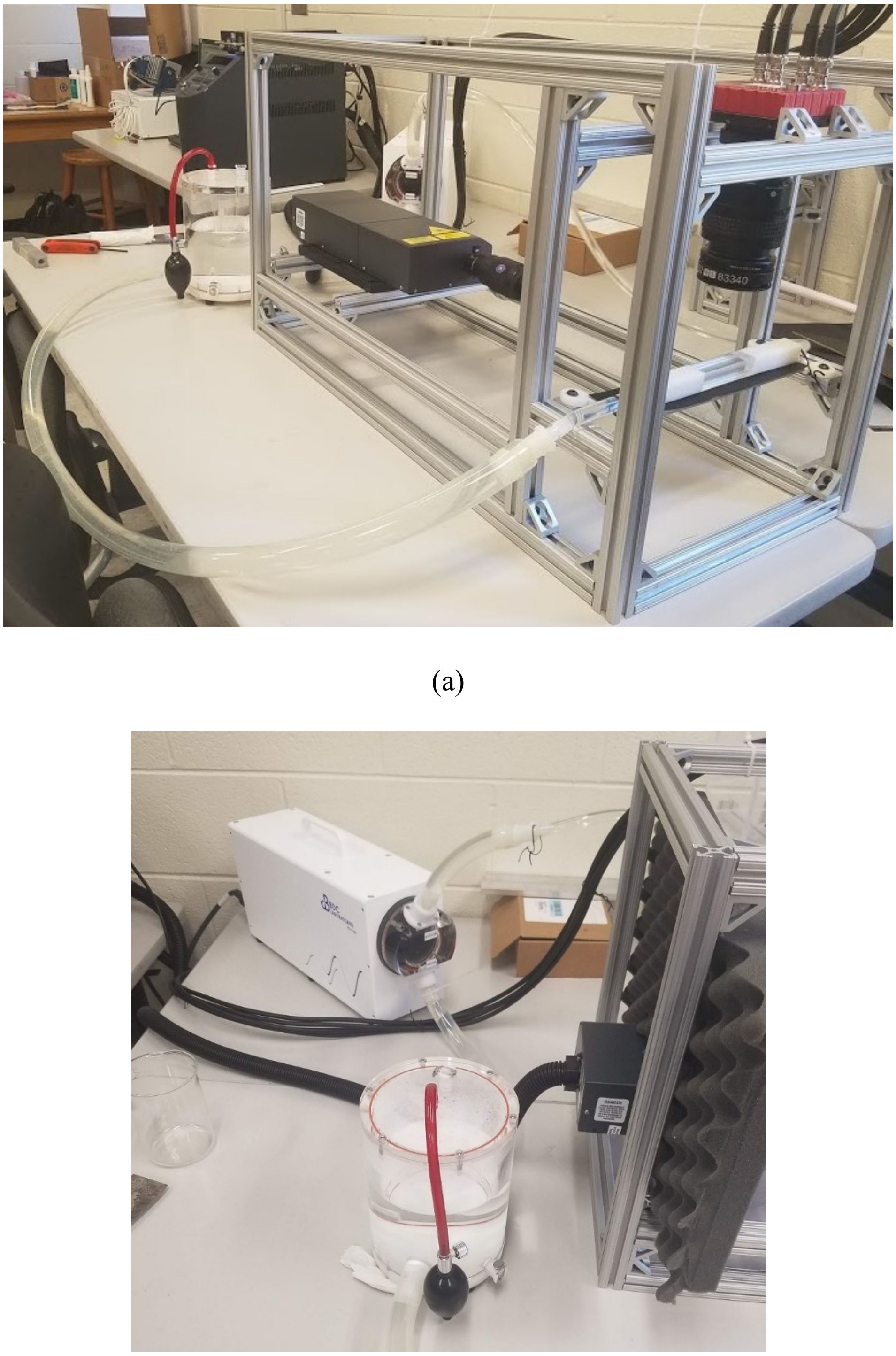

(a)

(b)

Figure 3.12: (a) PIV System (b) Pulsatile Pump and Compliance Chamber

The same flow loop and PIV setup used in the transient test sample experiments were used to acquire PIV images and measurements in the carotid bifurcation model. Similar to the test sample, a clear 3-D printed section was adhered to the arterial model to satisfy the entrance length for fully developed flow. An additional 3-D printed y-shaped junction was added at the exits to merge the exiting fluid back to one pipe to be routed to the compliance chamber. A photo of the model with the entrance and exit additions are shown below in *Figure 3.13 (a*). *Figure 3.13 (b)* presents the diseased section of the artery and the region of interest in which PIV measurements are obtained.

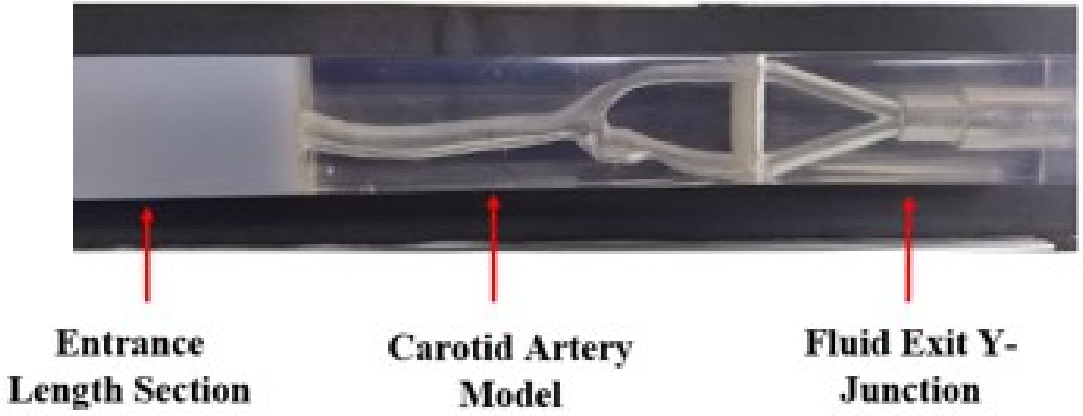

(a)

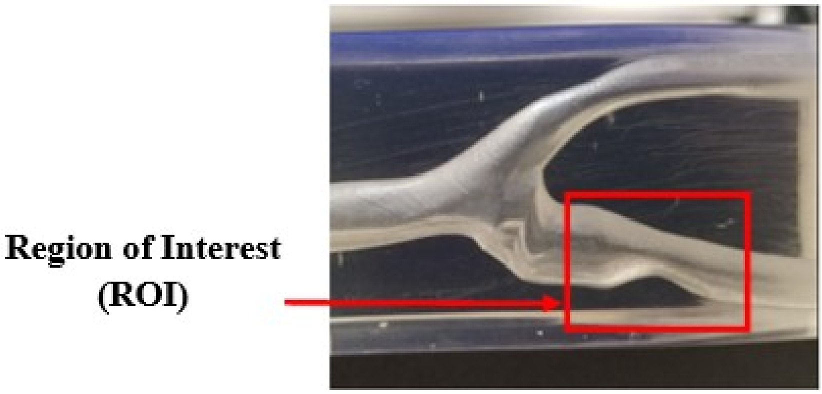

(b)

Figure 3.13: 3-D Printed Carotid Bifurcation Model: (a) Fully Assembled Model with Entrance and Exit Sections and (b) Stenosis Region of Interest

The same volumetric flow waveform and frequency was used in the transient arterial PIV experiment as the test sample. High-quality PIV images and velocity field measurements were obtained using the polished test sample as shown in *Figure 3.14.*

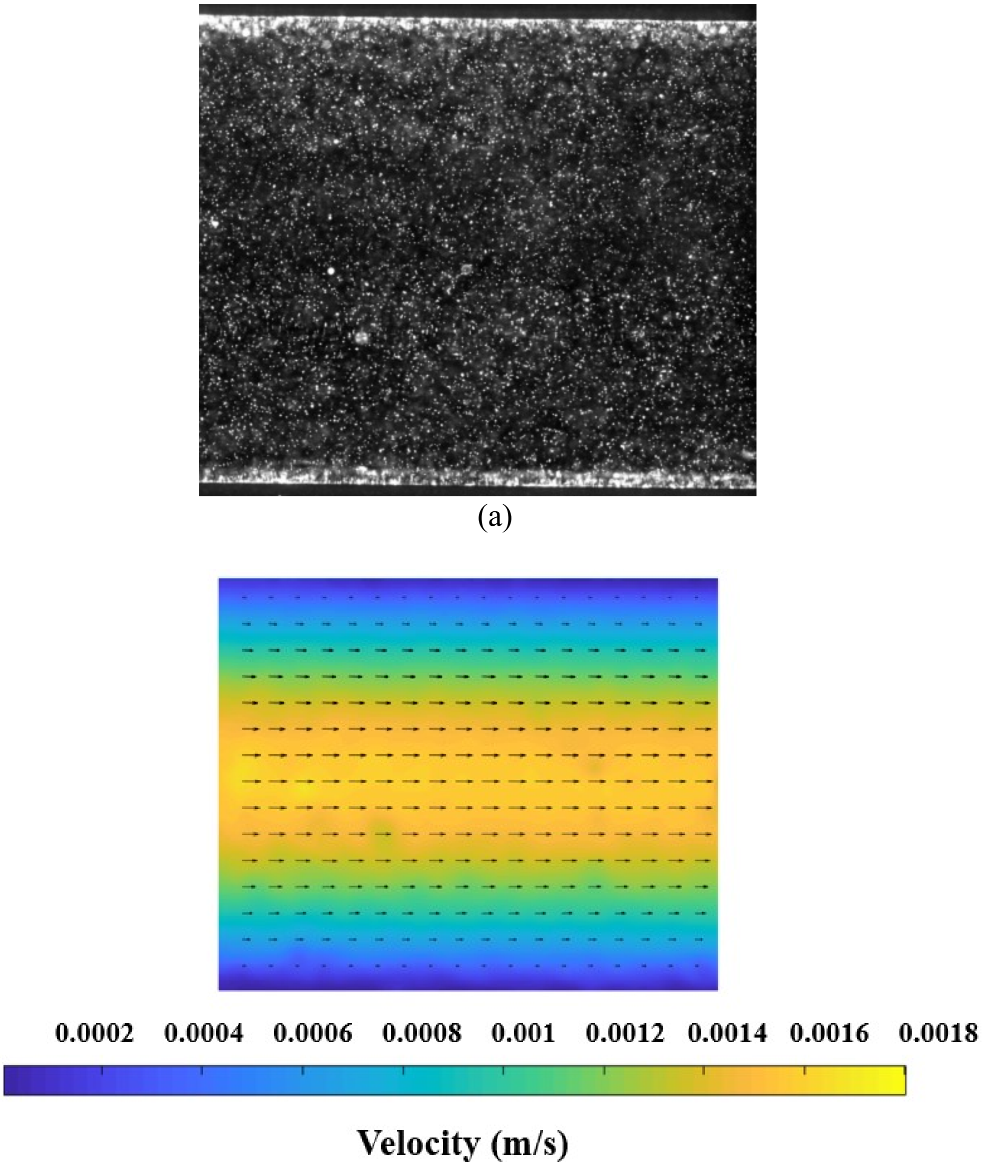

(a)

(b)

Figure 3.14: Test Sample PIV Results: (a) PIV Raw Image, (b) PIV Velocity Vector and Contour Plot

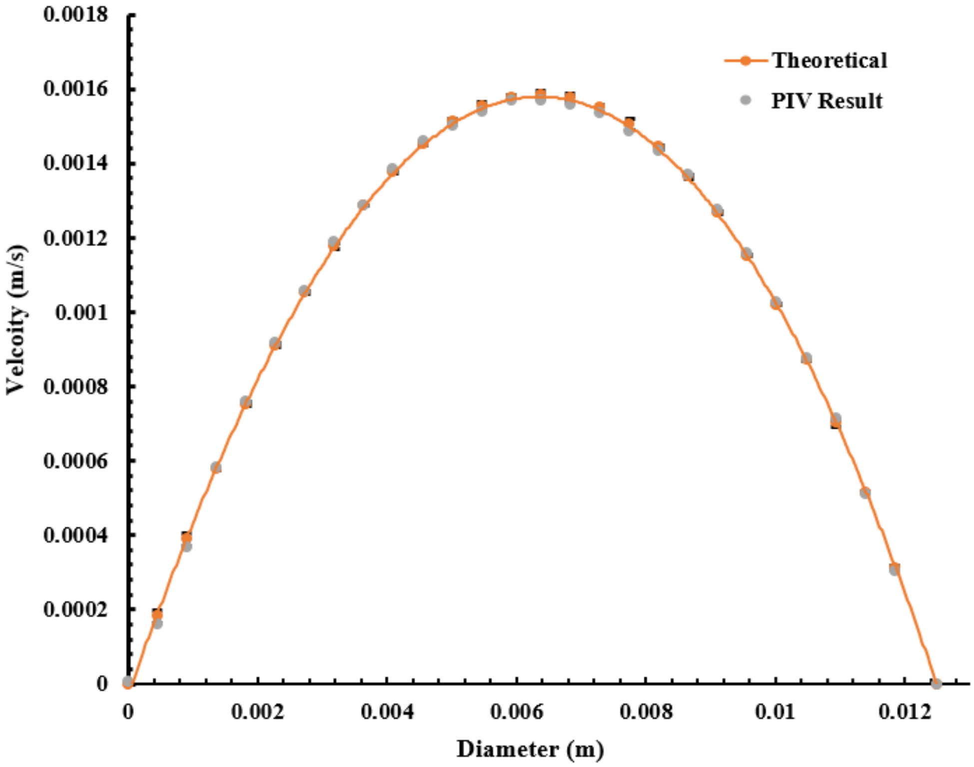

Figure 3.15: Test Sample PIV Results: Velocity Profile

After performing image post processing and cross-correlation, the velocity data was averaged to obtain the mean velocity field contours as shown in *Figure 3.14 (b)*. The flow was observed to be steady with relatively small variations in the velocity along the centerline as shown in *Figure 3.14 (b)*. The theoretical velocity profile obtained from the Poiseulli equation was compared to the velocity profile obtained from the PIV images as shown in *Figure 3.15*. Standard deviations were calculated from the theoretical and PIV results and showed minimum error due to the clarity of the part as shown *in Figure 3.15*.

CHAPTER 4: RESULTS AND DISCUSSION

4.1 Numerical Results

4.1.1 Blood Flow Results

The ability to target particles in the cardiovascular system is dependent on the capability of overcoming the hydrodynamic drag produced by cardiovascular flow. Also, it is evident that cardiovascular flow is highly unsteady, which has a huge effect on hemodynamic parameters. The flow characteristic profile inside the stenosed carotid bifurcation artery is shown in *Figure 4.1* for both systole and diastole during cycle 3 of the cardiac flow waveform. Contours of axial velocities have been plotted along eight sliced planes normal to the direction of flow. Flow streamlines representing the trajectory of finite fluid particles are tracked and superimposed on the transparent mesh and the axial velocity contours. As depicted in slice 3 of both diastole and systole, a Womersley flow profile is established upstream of the sinus bulb region of slice 3 and continues throughout the artery for both cases in the cardiac cycle observed. During diastole the flow is highly skewed towards the wall as shown in each axial velocity contour. The streamlines are also disorganized in the common carotid artery (CCA) region and show areas of flow separations and secondary flow upstream of the internal and external carotid artery (ICA and ECA). Similar findings have also been reported, whereby such skewed flow structure is primarily caused by the misalignment of the mean axis of the artery, curvature of the lumen, unsteady centrifugal forces caused by the sudden decrease and increase in flow velocity (Buchmann, 2011; Cheung, 2011; Vetel, 2009).

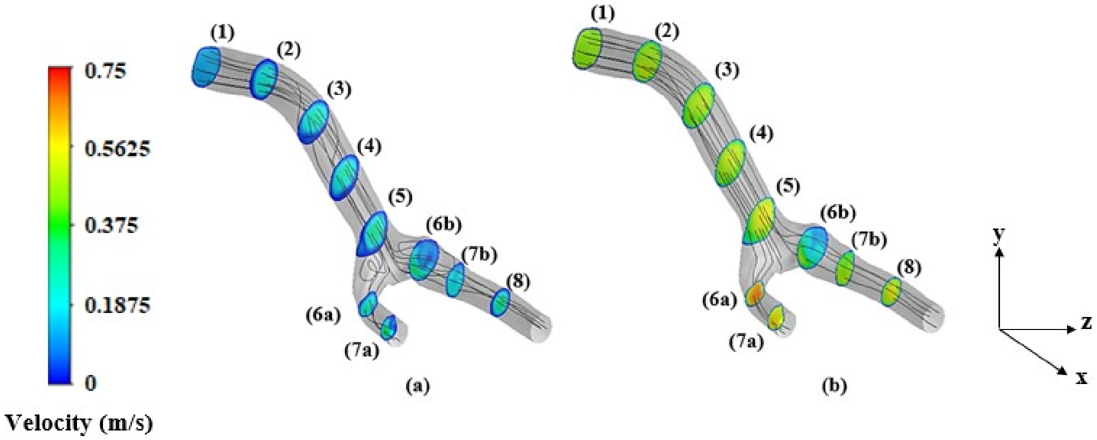

Figure 4.1: Contour Plots of Velocity and Streamline Traces of Blood Flow During (a) Diastole and (b) Systole (3rd Cardiac Cycle)

The asymmetric flow pattern within the stenosed carotid artery plainly depicts strong unsteadiness *(not to be confused with turbulence as the Re=545)* downstream of the sinus, while remaining flow dampens upstream of the sinus region. During diastole, fewer velocity profiles appear to have a Womersley profile and the streamlines are much more organized. This is believed to be due to the large momentum increase of fluid motion from systole to diastole in which the flow has achieved maximum flow. The sinus bulb region remains to have a Womersley profile which indicates that possibly some recirculating flow occurs in this region. A more conclusive examination can be predicted from a plot of the vorticity fields as shown in *Figure 4.2.*

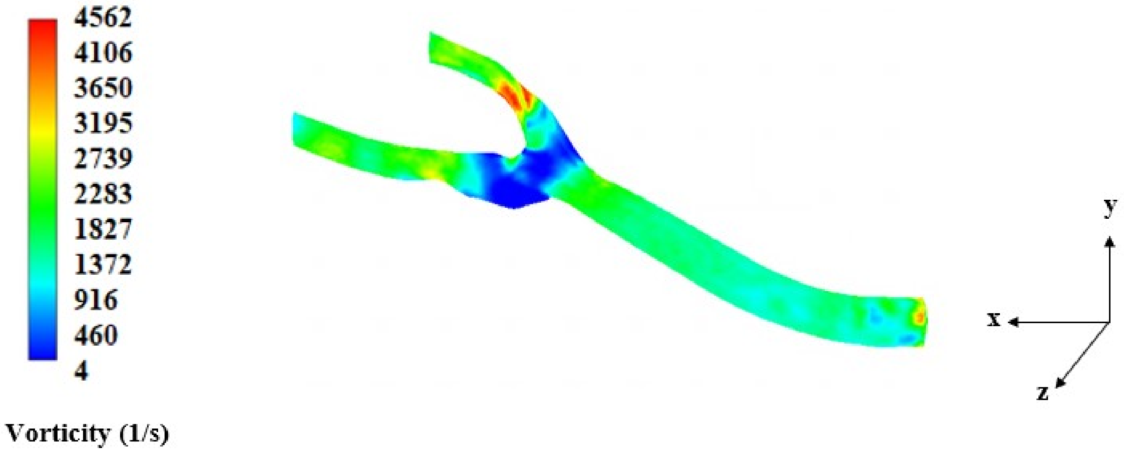

Figure 4.2: Contour of Flow Vorticity at Systole

As shown in *Figure 4.2*, from the bifurcation region to both the ICA and ECA, the flow changes significantly and becomes more chaotic with pronounced vorticial coherent structures and strong central vortex threading being formed through the stenosed regions of both branches. These unsteady affects also effect WSS as shown in *Figure 4.3*. The average range of WSS in the carotid artery is 1-12Pa (Sui, 2008; Xiao, 2018), whereas in the present work the highest WSS occurs around 18.93Pa at the stenosed region, indicating high near wall forces. The break-down of vortex structure in the post-stenotic region can also be observed. Flow separating areas that produce chaotic flow present huge barriers for particle targeting and capture. Moreover, the likely hood of particles sticking to the wall and remaining to the wall are highly unlikely without the presence of a magnetic field and during weak magnetic fields ($B_r > 1$T). In this case, the magnitude of hydrodynamic drag should be taken into consideration.

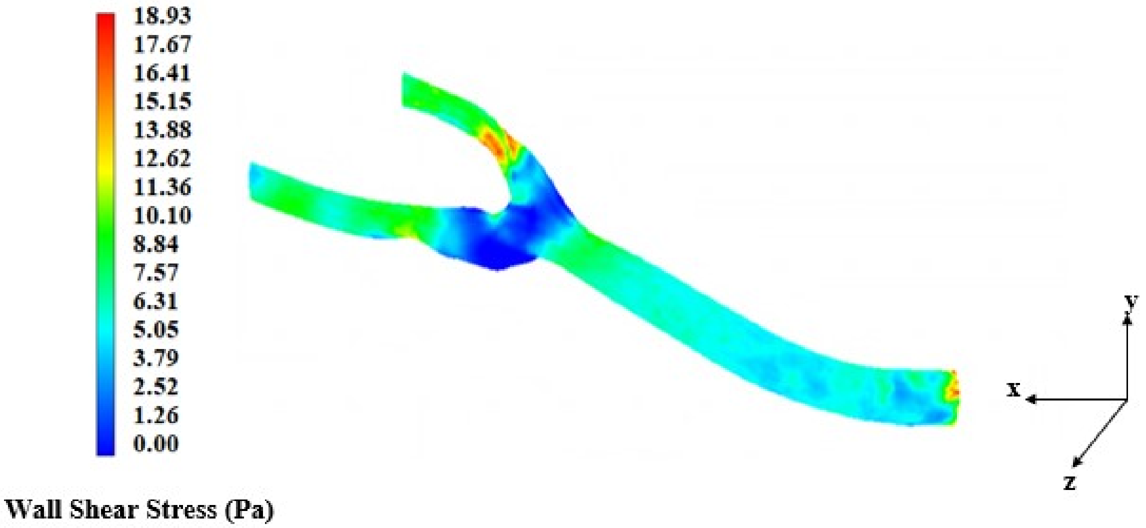

Figure 4.3: Wall Shear Stress Contours at Systole

In the present work, particles with diameters ranging from 20 nm to 4μm are uniformly injected into the flow through the inlet and subjected to the external magnetic field. The calculated drag forces that occur on particles ranging from 20nm to 4μm are of the range 0.025-12.48 pN. This indicates that a magnetic force must be generated higher than 12.48pN to overcome the hydrodynamic drag.

4.1.2 Particle Flow and Capture Results

Pulsatile blood flow simulations with a periodic inlet velocity boundary condition were performed in which the particles were uniformly injected at the inlet face at time increments of 1/100th of the flow over a total time of 3.2s. Over a time of 3.2s, a homogeneous mixture of 73,184 magnetite particles were uniformly injected into the artery from the inlet. *Figure 4.4* shows an interior view of the injected particles inside the carotid bifurcation artery downstream of the bifurcation point with the magnet turned off. The particles are colored by size and are scaled by 100 times the actual diameters.

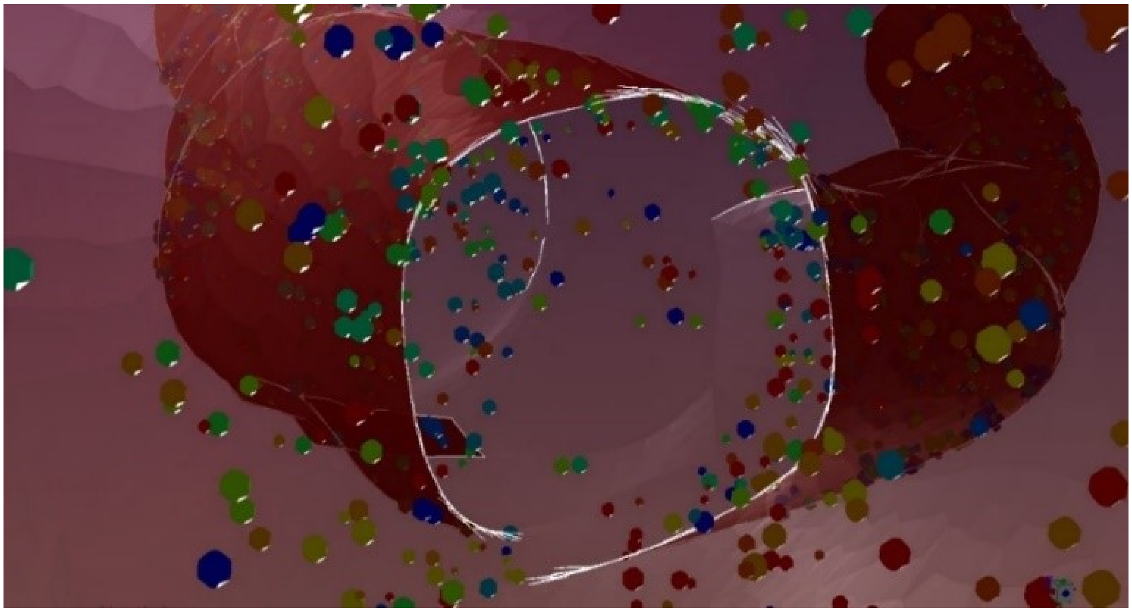

Figure 4.4: Interior View of Dispersed Particles Inside the Carotid Bifurcation Artery Downstream of the Bifurcation Point and Sinus Bulb

The magnitude of the magnetic field strength within the flow field for cases when the magnet is turned on is shown in *Figure 4.5.* The black circle represents the magnet and the dashed line represents the region of interest (ROI). The average magnetic field strength within the ROI site, specifically the sinus bulb and stenosed region (upstream and downstream) is approximately 0.571T. The magnitude of the force field generated by the magnetic field for 4μm diameter particles dispersed in the flow field is shown in *Figure 4.6*. The black circle represents the magnet and the dashed line respresents the region of interest (ROI). The average force within the ROI site, specifically the sinus bulb and stenosed region is approximately 12.4 pN.

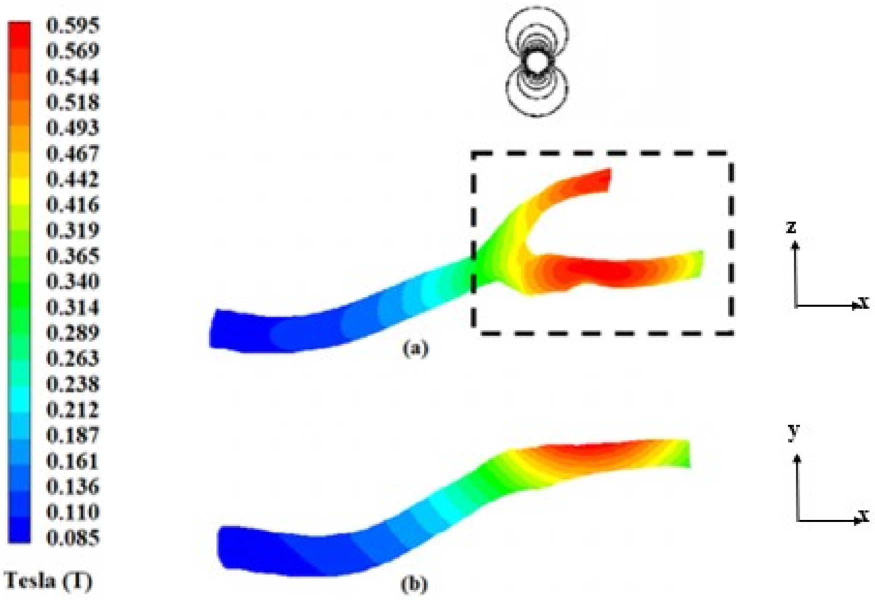

Figure 4.5: Contour of the Arterial Magnetic Field Strength at Br=2.0T (a) Top View and (b) Bottom View Generated in ANSYS Fluent

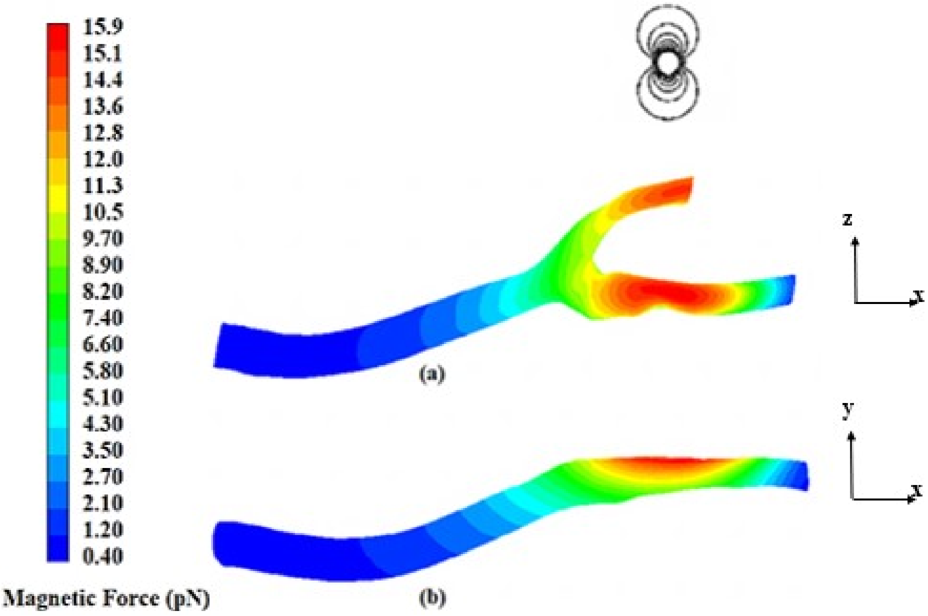

Figure 4.6: Contour of the Magnetic Pulling Force (Towards the Magnet) Exerted on 4µm Diameter Particles at Br=2.0T (a) Top View and (b) Bottom View Generated in ANSYS Fluent

A comparison analysis was conducted to illustrate the particle capture behavior for a normal artery vs. a diseased artery case. The same artery mentioned earlier was modified whereby the stenosis was removed to create an unrestricted flow boundary along the axial direction of where the stenosis was originally. This model is referred to as the normal artery, whereby the artery with the stenosis is referred to as the diseased artery. For both cases, particles were injected through the inlet face of the artery over a total time of 0.8 s with the magnet turned off. After 0.8 s, the magnet was turned on and simulations were ran over a total time of 3.2 s. *Figure 4.7* shows a top view (view from the bottom of the magnet facing the artery) of the particles dispersed in the normal artery during studies in which the magnet is turned off and for a case in which the magnet is turned on. *Figure 4.8* also shows the same scenario for the diseased artery case.

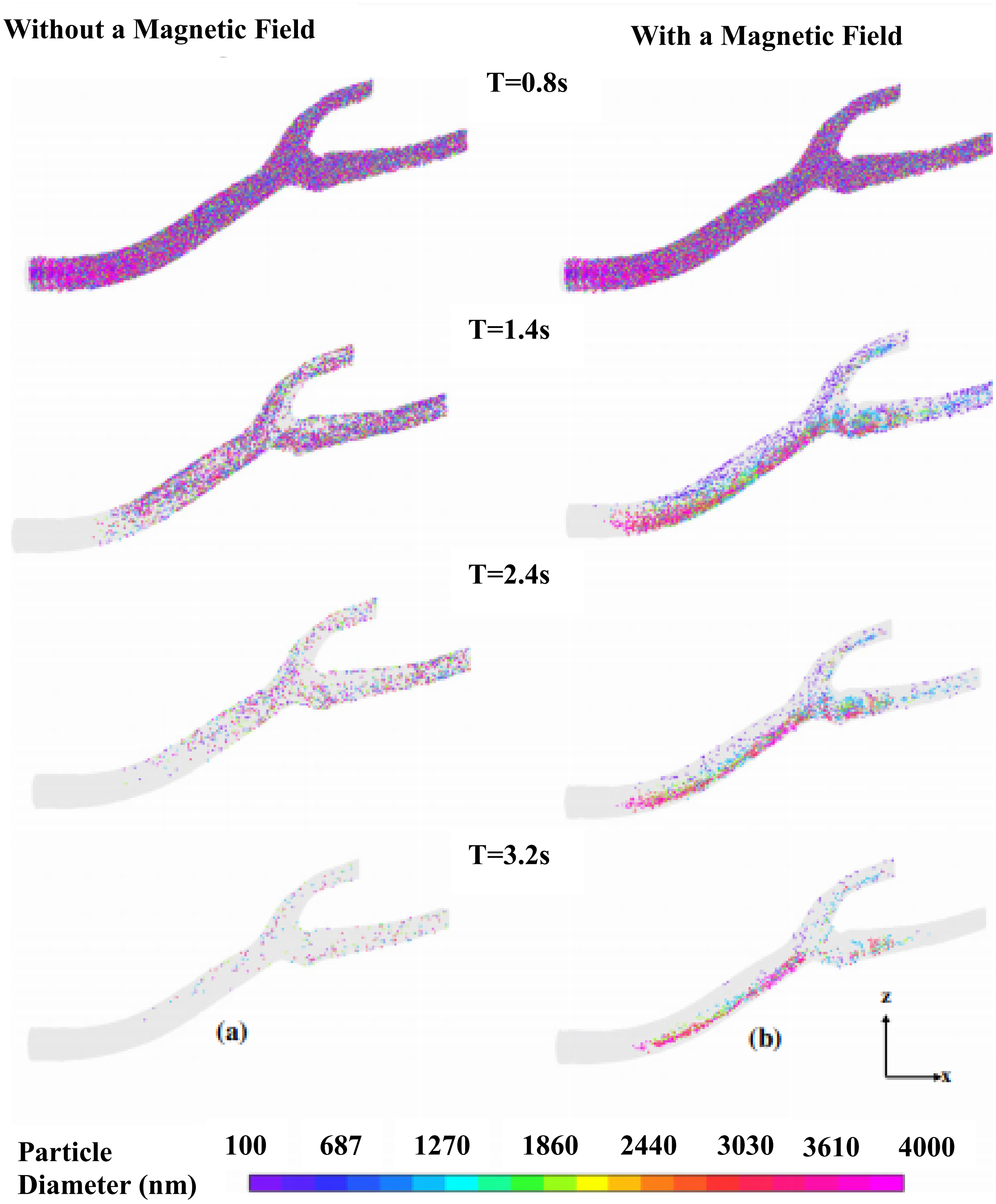

Figure 4.7: Particle Distribution in the Normal Carotid Artery at Different Time Instances (a) Without a Magnetic Field and (b) With a Magnetic Field Turned on at 0.8 s and for the Duration of the Tracking

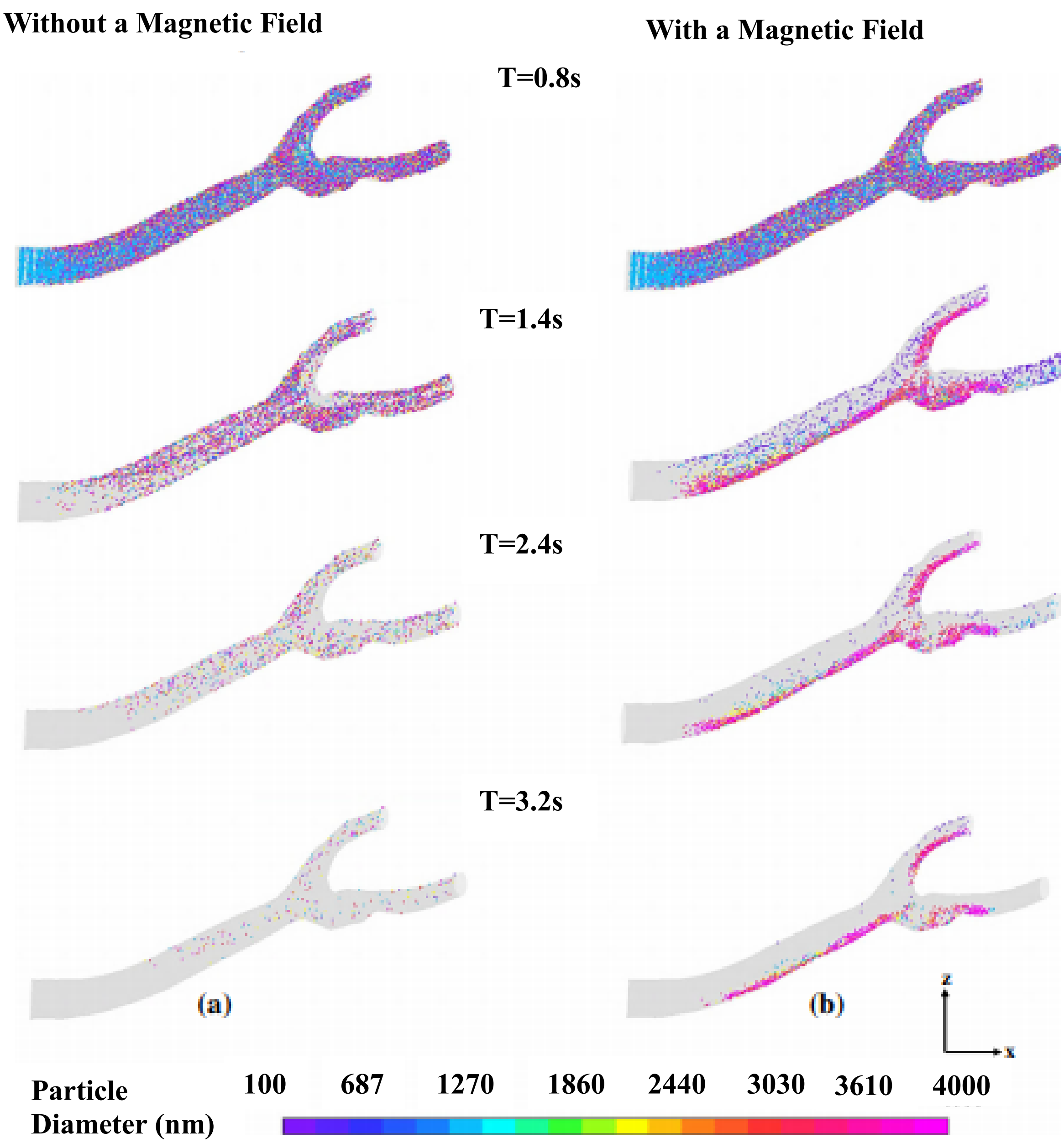

Figure 4.8: Particle Distribution in the Diseased Carotid Artery at Different Time Instances (a) Without a Magnetic Field and (b) With a Magnetic Field Turned on at 0.8 s and for the Duration of the Tracking

For both the normal and diseased artery cases, during the time when the magnet is turned off, the particles are injected into the artery and flow throughout the artery due to the viscous drag force produced by the driving pressure wave as shown in both *Figure 4.7* *(a) and Figure 4.8 (a)*. The particles follow the flow streamlines as their inertia is negligible compared to the viscous drag. As shown in both *Figure 4.7 (a) and Figure 4.8 (a)*, over a total time of 3.2 s, the majority of particles have exited the artery and only a few particles are found to adhere to the vessel walls due to the no slip condition. When the magnet is turned on, as shown in both *Figure 4.7 (b) and Figure 4.8 (b)*, the particles are found to be influenced appreciably by the magnetic force. For both the normal and diseased artery cases, the particles are shown to be attracted to the top portion of the vessel wall where they can exchange medical drugs with the arterial wall. For the diseased case however, the particles are shown to be skewed towards the top edge of the vessel wall. This phenomenon is illustrated in *Figure 4.9*.

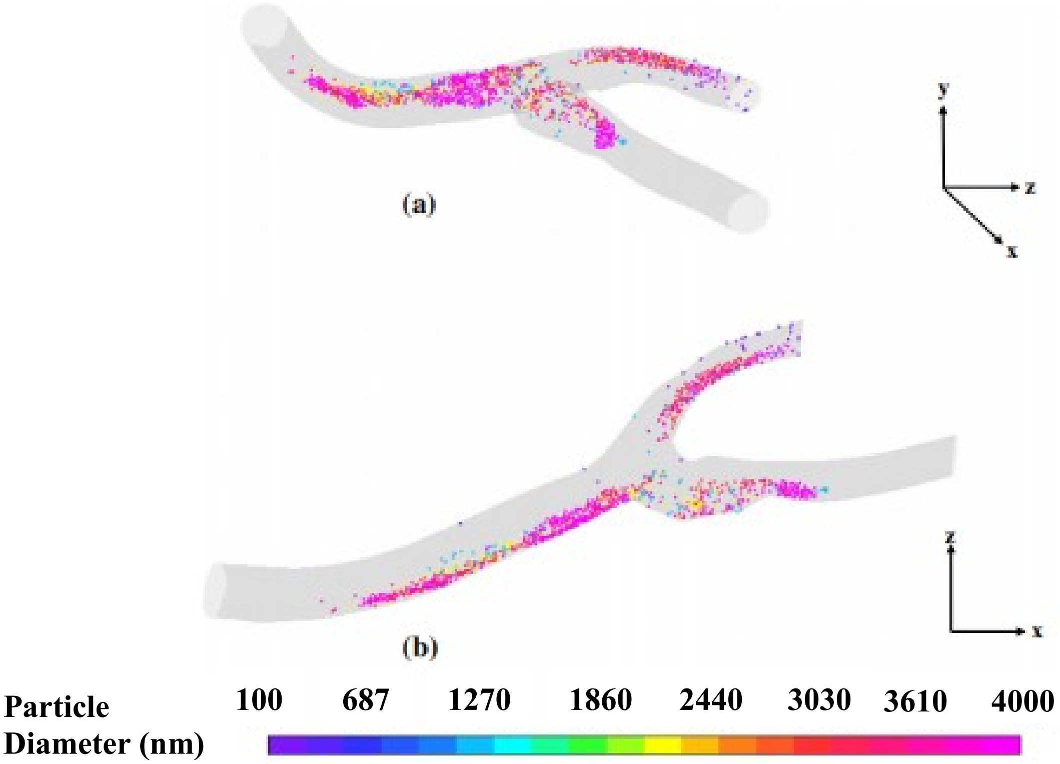

Figure 4.9: Particle Distribution of Captured Particles in the Diseased Carotid Artery at 4 s (Br= 2T) (a) Isometric View and (b) Top View

As mentioned previously, the flow is axisymmetric in nature and the magnetic arrangement does not show angular or axial symmetry. For both cases, the majority of particles tend to be attracted to regions where recirculation is low. For the normal artery case, particle dispersion and capture appear to be balanced (equal) on both the ICA and ECA as compared to the diseased case at time 1.6 s in *Figure 4.7 (b)*. This is believed to be attributed to the fact that the lack of a stenosis on the ICA branch promotes smoother flow and equalized velocity distributions on both branches which allow a more balanced transport of particles on both branches. This phenomenon also encourages the capture of smaller micron sized particles as shown in *Figure 4.7 (b)* for time 3.2 s.

For the diseased artery case, no particles are captured near the inner edge of the stenosed region. The inner edge of the stenosed region is a high recirculation zone and area where the Venturi effect causes a significant increase in velocity and makes particle capture difficult. However, when considering the capture efficiency in terms of particle diameter, a significant fraction of the captured particles is 4 μm in diameter. Similar results have been reported in previous studies (Bose, 2014) (Lunnoo & Puangmali, 2015). This deems to be a positive result when considering *ex vivo* applications for MDT to large arterial sections. The overall capture efficiency of the homogeneous dispersion was found to be 77% for the diseased artery case. The overall capture efficiency of the homogenous dispersion for the normal artery case was 68%. In comparison, the normal artery allows more particles to escape overtime as compared to the diseased case due to the lack of a stenosis. For the diseased case, a capture efficiency quantitative analysis was conducted for homogenous dispersions of particle diameters ranging from the superparamagnetic region to 4 μm as shown in *4.10 Plot of Capture Efficiency as a Function of Particle Diameter and Varying Magnetic Field Strength in the Carotid Artery.*

4.10 Plot of Capture Efficiency as a Function of Particle Diameter and Varying Magnetic Field Strength in the Carotid Artery shows the calculation result for MDT capture efficiency as a function of particle diameter and varying magnetic field strength. The first observation is that the best capture efficiency results at Br= 2.0T as compared to lower magnetic field strengths. The second observation is that the larger diameter particles (micron sized particles) have better cumulative capture efficiency and targeting potential compared to smaller diameter particles (superparamagnetic particles). For the best capture efficiency case which occurs at Br= 2.0T, high capture efficiencies of 92–98% were observed for particles larger than 1 μm in diameter. For particles with diameters ranging from 500 to 800 nm, capture efficiencies of 60–91% were observed. For smaller particles ranging from the superparamagnetic regime to 400 nm, capture efficiencies of 0.5–30% were observed. As reported in previous studies, for *in vivo* applications and depending on the medical injection location, large particles (D > 200 nm) may be quickly eliminated by the reticuloendothelial system of the spleen and liver during continuous circulation in the cardiovascular system (Lunnoo & Puangmali, 2015) (Shubayev, 2009). Smaller particles (10–200 nm) in diameter have been reported to be optimal for *in vivo* MDT as they can escape renal clearance, whereas the large particles are eliminated.

It is worth mentioning that the smaller diameter particles will flow past the magnetized region of interest again as they circulate continuously in the bloodstream for an *in vivo* case. The overall capture efficiency of smaller particles may potentially increase during an *in vivo* case through many passes, contrary to what is shown in *4.10 Plot of*

Capture Efficiency as a Function of Particle Diameter and Varying Magnetic Field Strength in the Carotid Artery.

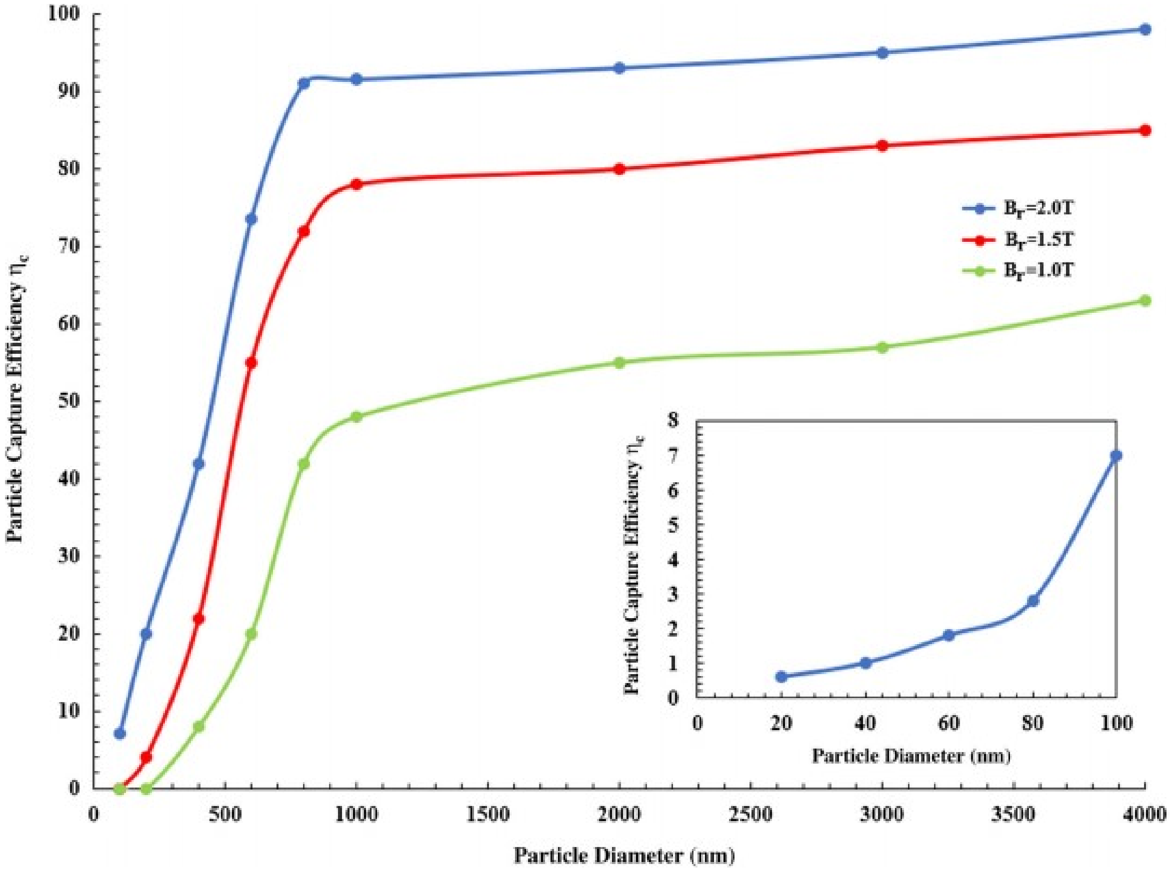

Figure 4.10: Plot of Capture Efficiency as a Function of Particle Diameter and Varying Magnetic Field Strength in the Carotid Artery

4.2 Experimental Results

As shown in *Figure 4.11 (a)*, a Womersley velocity profile is established in which the flow is highly skewed towards the wall. This is also shown in the extracted velocity profile shown *in Figure 4.11 (b)*. The velocity also appears to vary along the centerline of the test sample. This could be attributed to pulsatile pressure wave and high centrifugal forces cause by the curving in the flexible tubing that delivers fluid from the pump to the test section.

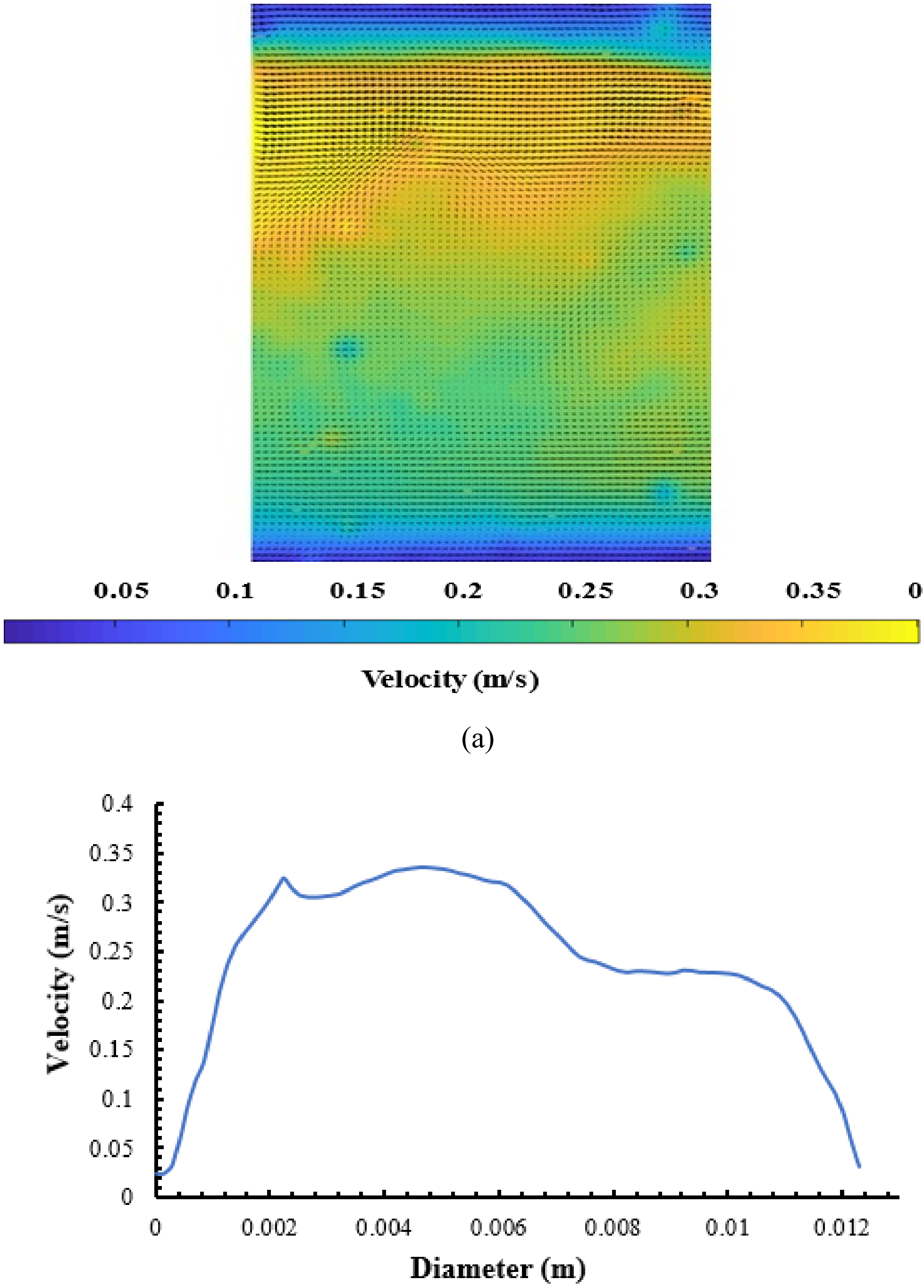

(a)

(b)

Figure 4.11: Test Sample Transient PIV Results: (a) Velocity Contour and (b) Extracted Center Velocity Profile

Figure 4.12 (a) presents the raw PIV image, *Figure 4.12 (b)* presents the velocity vector field and streamlines, and *Figure 4.12 (c*) presents the velocity profile that was obtained from the transient arterial experiment. As shown in *Figure 4.12 (b)*, the highest velocity magnitude occurs at the stenosis section and continues throughout the branch of the ICA. The high magnitude of velocity occurs due to the Venturi effect caused by the restriction at the stenosis (ROI). The continuation of this trend occurs due to the varying diameter along the ICA branch centerline. The streamlines shown in *Figure 4.12 (b*) demonstrates areas of strong unsteadiness and vortex shedding at the sinus bulb and recirculation upstream of the stenosis near the wall. As shown in extracted velocity profile at the ROI in *Figure 4.12 (c)*, the no slip condition is not captured. This is partially attributed to the varying curvature, scattering of light, and the varying plane along the axis of both the ICA and ECA branch centerline.

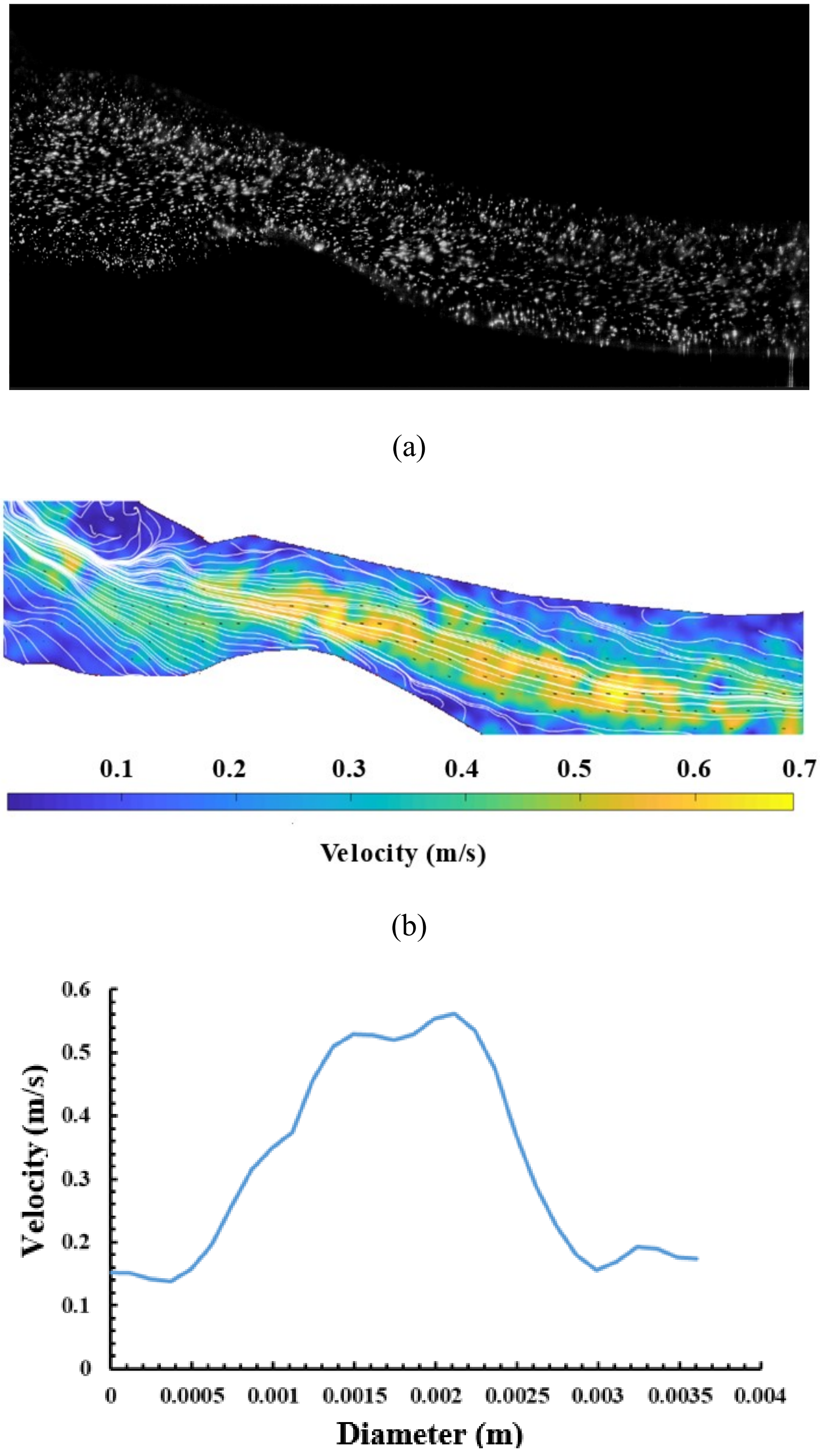

(a)

(b)

(c)

Figure 4.12: Carotid Artery Transient PIV Results: (a) Raw PIV Image, (b) Velocity Vector Field, Contour, and Streamlines, and (c) Extracted Velocity Profile at the Center of the ROI

CHAPTER 5: CONCLUSION

5.1 Numerical

Three-dimensional modelling of pulsatile blood flow, particle motion, and particle tracking was performed in a patient-specific diseased left carotid bifurcation artery using the magnetic properties of magnetite (Fe_3O_4) and equations describing the forces acting on particles produced by an external cylindrical electromagnetic coil. A two-way coupled (fluid and particle coupled) Eulerian–Lagrangian technique was adopted and implemented to resolve the hemodynamic flow and the motion of particles under the influence of a magnetic field (B_r = 2T). The computational simulations demonstrate that the greatest particle capture efficiency result for particle diameters within the micron range, specifically 4 μm in regions where flow separation and vortices are at a minimum. It was also determined that the capture efficiency of particles decreases substantially with particle diameter, especially in the superparamagnetic regime. It is also worth noting that several simplifications have been introduced in the computational simulations involving the vessel geometry, boundary conditions, and particle modeling.

Some of these simplifications include restructuring portions of the arterial model that promote meshing irregularities, modelling the vessel as a rigid wall vessel, implementing a velocity inlet waveform that does not match the true waveform of the subject being studied, and not modelling the drug thickness on particles. It is unlikely that improvements in these simplifications will severely alter the capture efficiency results significantly. Perhaps the most significant simplification was made by evaluating the drag force for superparamagnetic particles via Stokes expression, using the Carreau nonNewtonian fluid viscosity model. The Carreau fluid viscosity model projects a significantly higher viscosity than the actual viscosity of blood plasma. In this case, small particles within the superparamagnetic regime may tend to move along stream traces in the blood plasma without colliding with blood constituents, therefore experiencing a drag force proportional to the viscosity of the blood plasma. The viscous drag experienced by particles of the order of or smaller than the blood cells, as used in the present work, may therefore be much smaller than that which is presently used by considering the Carreau viscosity model. This could significantly change the outcome of capture efficiency for superparamagnetic particles in computational simulations such as those presented in the present work. The obtained capture efficiency results for the superparamagnetic could be significantly underestimated.

In addition, the authors would like to mention that an alternative approach for increasing capture efficiency of smaller particles in larger arteries may be done potentially by modeling a magnetized cardiovascular stent in the diseased sections as opposed to targeting particles in diseased sections of the artery during pre-stenting. In this case, the magnetized stents could potentially amplify the magnetic field gradient and increase particle capture of superparamagnetic particles. Future studies should explore experimentally and numerically, the effect of a secondary magnetic field produced by a magnetized stent on capture efficiency. Computational simulations such as those discussed in the present work make it possible to study the feasibility and practicality of MDT a prior to clinical trials. Furthermore, computational simulations are useful for investigating the influence of various factors independently and for optimization. The simulations results presented in the present work have shown to yield favorable capture efficiencies for micron range particles and a potential for enhancing capture efficiency of superparamagnetic particles in smaller arteries and/or using magnetized implants such as cardiovascular stents. The present work presents results for justifying further investigation of MDT.

5.2 Experimental

The experiments described in the present work indicate that 3-D printing may be used to produce rigid optically clear simple and complex anatomical models that are appropriate for PIV analyses. The main limitations of the rapid prototyping of 3-D printed rigid arterial vessel models as described herein is the need to manually post process vessel models via soaking, wet sanding, and polishing the inner and outer surfaces of the anatomical vessels. Despite these limitations, the approach described in the present work for fabricating complex optically clear arterial models is well suited for PIV measurements.

The steady flow observed in the test sample had relatively small variations in the velocity along the centerline as expected from the numerical simulations. The theoretical velocity profile obtained from the Poiseulli equation was also compared to the velocity profile obtained from the PIV images and the standard deviations were calculated from the theoretical and PIV results. There was minimum error due to the clarity of the flow conduit. After the pulsatile pump was attached for unsteady flow, a Womersley velocity profile was established in which the flow is highly skewed towards the wall. The velocity also appears to vary along the centerline of the test sample. This could be attributed to pulsatile pressure wave and high centrifugal forces cause by the curving in the flexible tubing that delivers fluid from the pump to the test section. The no-slip condition is also not captured at the wall of the test sample which could be attributed to light scattering from the laser to the fluorescent particles and blurring at the wall.

The same flow loop and PIV setup used in the transient test sample experiments were used to acquire PIV images and measurements in the carotid bifurcation model. The highest velocity magnitude occurred at the stenosis section (ROI) and continued throughout the branch of the ICA. The high magnitude of velocity occurred due to the Venturi effect caused by the restriction at the stenosis (ROI). The continuation of the trend was due to the varying diameter along the ICA branch centerline. The acquired streamlines demonstrated areas of strong unsteadiness and vortex shedding at the sinus bulb and recirculation upstream of the stenosis near the wall. The no slip condition was captured partially because of the varying curvature, scattering of light, and the varying plane along the axis of both the ICA and ECA branch centerline. Post processing the inside of the 3-D printed carotid artery could result in more clear PIV results allowing for capturing of the no slip condition at the wall.

5.3 Further Research

Future work should explore measuring surface roughness of the interior part of the 3-D printed arterial models and possibly exploring the possibility of using techniques such as vapor deposition smoothing to rectify high surface roughness which could promote glaring and undesired frictional energy losses. Future work should also involve comparing the PIV results of the 3-D printed rigid arterial model to a compliant model of the same geometry under the same conditions, as shown in *Appendix C: Compliant Arterial Model*.

The next steps to continue this research should be implementing the inlet velocity UDF wave into the pulsatile pump to generate the same inlet velocity used in the numerical simulations for PIV experiments. After comparing the results using the same wave form, a method of measuring particle capture efficiency experimentally should be developed for experimental MDT studies. The numerical and experimental efficiencies should be compared before developing a system to use and validate MDT experimentally to compare to the numerical results previously gathered.

REFERENCES

Agiotis, L., Theodorakos, I., Samothrakitis, S., Papazoglou, S., Zergioti, I., & Raptis, Y. S. (2016). "*Magnetic Manipulation of Superparamagnetic Nanoparticles in a Microfluidic System for Drug Delivery Application"s*. *Journal of Magnetism and Magnetic Materials, 401*, 956-964. doi:10.1016/j.jmmm.2015.10.111

Ajkidkarn, P., Ritprajak, P., Injumpa, W., Porntaveetus, T., & Insin, N. (2017). *"Synthesis, Characterization, Drug Release and Transdentinal Delivery Studies of Magnetic Nanocubes Coated with Biodegradable Poly 2-(Dimethyl Amino) Ethyl Methacrylate". Journal of Magnetism and Magnetic Materials, 427*, 235-240. doi:10.1016/j.jmmm.2016.11.020

Alexiou, C., Jurgons, R., Schmid, R., Hilpert, A., Bergemann, C., Parak, F., & Iro, H. (2005). "*In vitro and in vivo Investigations of Targeted Chemotherapy with Magnetic Manoparticles*". *MAGMA Journal of Magnetism and Magnetic Materials, 293*(1), 389-393.

Alexiou, C., Tietze, R., Schreiber, E., Jurgons, R., Richter, H., Trahms, L., Lyer, S. (2011). *"Cancer Therapy with Drug Loaded Magnetic Nanoparticlesmagnetic Drug Targeting". MAGMA Journal of Magnetism and Magnetic Materials, 323*(10), 1404-1407.

Allard, L., Soulez, G., Chayer, B. (2009). *"Multimodality Vascular Imaging Phantoms: A New Material for the Fabrication of Realistic 3D Vessel Geometries". Medical Physics, 36*(8), 3758-3763.

Association, A. H. (2017). "*Heart Disease and Stroke Statistics 2017 At-a-Glance*".

Bluestein, D., Niu, L.J., Schoephoerster, R.T., et al. (1997). *"Fluid Mechanics of Arterial Stenosis: Relationship to the Development of Mural Thrombus". Annals of Biomedical Engineering, 25*(2), 344-356.

Boghi, A., Russo, F., & Gori, F. (2017). *"Numerical Simulation of Magnetic Nano Drug Targeting in a Patient-Specific Coeliac Trunk". Journal of Magnetism and Magnetic Materials, 437*, 86-97. doi:10.1016/j.jmmm.2017.04.055

Bose, S., Datta, A., Ganguly, R., and Banerjee, M. (2014). *"Lagrangian Magnetic Particle Tracking Through Stenosed Artery Under Pulsatile Flow Condition". J. of Nano. Eng. Med., 4*(3), 1-10.

Buchmann, A., C., Jeremy, M.C., and Soria, J. (2011). *"Tomographic Particle Image Velocimetry Investigation of the Flow in a Modeled Human Carotid Artery Bifurcation". Exp. Fluids, 50*(4), 1131-1151.

Büsen, M., Arenz, C., Neidlin, M., Liao, S., Schmitz-Rode, T., Steinseifer, U., & Sonntag, S. J. (2017). *"Development of an In Vitro PIV Setup for Preliminary Investigation* *of the Effects of Aortic Compliance on Flow Patterns and Hemodynamics". Cardiovasc Eng Tech Cardiovascular Engineering and Technology, 8*(3), 368-377.

Cao, Q., Han, X., & Li, L. (2011). *"Enhancement of the Efficiency of Magnetic Targeting for Drug Delivery: Development and Evaluation of Magnet System". MAGMA Journal of Magnetism and Magnetic Materials, 323*(15), 1919-1924.

Cherry, E. M., & Eaton, J. K. (2014). *"A Comprehensive Model of Magnetic Particle Motion During Magnetic Drug Targeting". International Journal of Multiphase Flow International Journal of Multiphase Flow, 59*(2), 173-185.

Cheung, S. C., Wong, K.K., Yeoh, G.H., et. al. (2011). *"Experimental and Numerical Study on the Hemodynamics of Stenosed Carotid Bifurcation". Australas. Phys. Eng. Sci. Med., 33*(4), 319-328.

Doyle, B. J., Cloonan, A.J., Walsh, M.T., et al. (2010). *"Identification of Rupture locations in Patient-Specific Abdominal Aortic Aneurysms using Experimental and Computational Techniques". J. Biomech, 43*, 1408-1416.

Formlabs. (2018). *"Index of Refraction". Formlabs Community Forum.*

Furlani, E. J., and Furlani, E.P. (2007). *"A Model for Predicting Magnetic Targeting of Multifunctional Particles in the Microvasculature". Journal of Magnetism and Magnetic Materials, 312*, 187-193.

Gates, P. E., Gurung, A., Mazzaro, L., et al. (2018). *"Measurement of Wall Shear Stress Exerted by Flowing Blood in the Human Carotid Artery: Ultrasound Doppler Velocimetry and Echo Particle Image Velocimetry". Ultrasound in Medicine and Biology, 44*(7), 1392-1401.

Gharahi, H., B. Zambrano, D. Zhu. (2016). *"Computational Fluid Dynamic Simulation of Human Carotid Artery Bifurcation Based on Anatomy and Volumetric Blood Flow Rate Measured with Magnetic Resonance". International Journal of Advances in Engineering Sciences and Applied Mathematics*.

Gitter, K., & Odenbach, S. (2011). *"Experimental Investigations on a Branched Tube Model in Magnetic Drug Targeting". Journal of Magnetism and Magnetic Materials, 323*(10), 1413-1416. doi:10.1016/j.jmmm.2010.11.061

Gleich, B., Hellwig, N., Bridell, H., Jurgons, R., Seliger, C., Alexiou, C., Weyh, T. (2007). *"Design and Evaluation of Magnetic Fields for Nanoparticle Drug Targeting in Cancer". IEEE transactions on nanotechnology., 6*(2), 164-170.

Ha, H., and Lee, S.J. (2014). *"Effect of Swirling Inlet Condition on the Flow Field in a Stenosed Arterial Vessel Model". Medical Engineering & Physics, 36*(1), 119-128.

Haider, A., and Levenspiel, O. (1989). *"Drag Coefficient and Terminal Velocity of Spherical and Nonspherical Particles". Powder Technology, 58*, 63-70.

Hajiaghajani, A., Hashemi, S., & Abdolali, A. (2017). *"Adaptable Setups for Magnetic Drug Targeting in Human Muscular Arteries: Design and Iimplementation". Journal of Magnetism and Magnetic Materials, 438*, 173-180. doi:10.1016/j.jmmm.2017.04.058

Hewlin, R. L., and Kizito, J. (2018). *"Development of an Experimental and Digital Cardiovascular Arterial Model for Transient Hemodynamic and Postural Change Studies: A Preliminary Analysis". Cardiovascular Engineering and Technology, 9*(1), 1-31.

Hopkins, J. T., Kelly, A.S., Wexler, A.K., et al. (2000). *"Particle Image Velocimetry Measurements in Complex Geometries". Exp. Fluids, 29*(1), 91-95.

Hoshiar, A. K., Le, T. A., Ul Amin, F., Kim, M. O., & Yoon, J. (2017). *"Studies of Aggregated Nanoparticles Steering During Magnetic-Guided Drug Delivery in the Blood Vessels". Journal of Magnetism and Magnetic Materials, 427*, 181-187. doi:10.1016/j.jmmm.2016.11.016

Huang, Y. S., Lu, Y. J., & Chen, J. P. (2017). *"Magnetic Graphene Oxide as a Carrier for Targeted Delivery of Chemotherapy Drugs in Cancer Therapy". Journal of Magnetism and Magnetic Materials, 427*, 34-40. doi:10.1016/j.jmmm.2016.10.042

Janikowska, A., Matuszak, J., Lyer, S., Schreiber, E., Unterweger, H., Zaloga, J., Cicha, I. (2017). *"A Novel Human Artery Model to Assess the Magnetic Accumulation of SPIONs Under Flow Conditions". Scientific reports, 7*.

Jiang, C. (2016). "*Fluent-3D Birfurcating Artery"*. Retrieved from https://confluence.cornell.edu/display/SIMULATION/FLUENT+-+3D+Bifurcating+Artery

Kaare H. Bønaa, Jan Mannsverk, Rune Wiseth, et. al, (2016)."*Drug-Eluting or Bare-Metal Stents for Coronary Artery Disease". The New England Journal of Medicine*.

Kenneth Aycock, P. H., Brent Craven. (2017). *"Particle Image Velocimetry Measurements in an Anatomical Vascular Model Fabricated Using Inkjet 3D Printing". Experiments in Fluids, 58*.

Lai, S. S., Yiu, B.Y., Poon, A.K., et al. (2009). *"Design of Anthropomorphic Flow Phantoms based on Rapid Prototyping of Compliant Vessel Geometries". UMB, 39*(9), 1654-1664.

Lockhart, C. J., Gamble, A. J., Rea, D., Hughes, S., McGivern, R. C., Wolsley, C., McVeigh, G. E. (2006). *"Nitric Oxide Modulation of Ophthalmic Artery Blood Flow Velocity Waveform Morphology in Healthy Volunteers". Clinical Science, 111*(1), 47-52. doi:10.1042/cs20050365

Lunnoo, T., & Puangmali, T. (2015). *"Capture Efficiency of Biocompatible Magnetic Nanoparticles in Arterial Flow: A Computer Simulation for Magnetic Drug*

Targeting". Nanoscale Research Letters, 10(1), 426. doi:10.1186/s11671-015-1127-5

McGloughlin, T. M., and Doyle, B.J. (2010). *"New Approaches to Abdominal Aortic Aneurysm Rupture Risk Assessment: Engineering Insights with Clinical Gain". Arterioscler Throm Vasc Biol, 30*, 1687-1694.

Mokhtar, N., Hafizah, A., Aizat, R., et al. (2017). *"Effect of Different Stent Configurations using Lattice Boltzmann Method and Particles Image Velocimetry on Artery Bifurcation Aneurysm Problem". Journal of Theoretical Biology, 433*, 73-84.

Momeni Larimi, M., Ramiar, A., & Ranjbar, A. A. (2016). *"Magnetic Nanoparticles and Blood Flow Behavior in Non-Newtonian Pulsating Flow within the Carotid Artery in Drug Delivery Application". Proc. Inst. Mech. Eng. Part H J. Eng. Med. Proceedings of the Institution of Mechanical Engineers, Part H: Journal of Engineering in Medicine, 230*(9), 876-891.

Mondal, A., & Shit, G. C. (2017). *"Transport of Magneto-Nanoparticles During Electro-Osmotic Flow in a Micro-Tube in the Presence of Magnetic Field for Drug Delivery Application". Journal of Magnetism and Magnetic Materials, 442*, 319-328. doi:10.1016/j.jmmm.2017.06.131

Morsi, S. A. a. A., A.J. (1972). "*An Investigation of Particle Trajectories in Two-Phase Flow Systems". Journal of Fluid Mechanics, 55*(2), 193-208.

Nacev, A., Beni, C., Bruno, O., & Shapiro, B. (2011). *"The Behaviors of Ferromagnetic Nano-Particles in and Around Blood Vessels Under Applied Magnetic Fields*". *Journal of Magnetism & Magnetic Materials, 323*(6).

Najjari, M. R., & Plesniak, M. W. (2018). *"Secondary Flow Vortical Structures in a 180° Elastic Curved Vessel with Torsion Under Steady and Pulsatile Inflow Conditions". Physical Review Fluids, 3*(1), 013101. doi:10.1103/PhysRevFluids.3.013101

Nguyen, T. T., Biadillah, R., Mongrain, J. et al. (2004). *“A Method for Matching the Refractive Index and Kinematic Viscosity of a Blood Analog for Flow Visualization in Hydraulic Cardiovascular Models". Journal of Biomechanical Engineering, 126*, 529-535.

Nicholas Stanley, A. C., William Timms, Rodward Hewlin Jr. (2019). "*Development of 3-D Printed Optically Clear Rigid Anatomical Vessels for Particle Image Velocimetry Analysis in Cardiovascular Flow". ASME International Mechanical Engineering Congress & Exposition, November 2019, Salt Lake City, Utah*.

NOVUS. (2011). "*Novus Plastic Polish"*. Retrieved from https://www.novuspolish.com/

Ounis, H., Ahmadi, G., and McLaughlin, J.B. (1991). *"Brownian Diffusion of Submicrometer Particles in Viscous Sublayer". Journal of Colloid and Interface Science, 143*(1), 266-277.

Ravichandran, M., Oza, G., Velumani, S., Ramirez, J. T., Vera, A., & Leija, L. (2017). *"Design and Evaluation of Surface Functionalized Superparamagneto-Plasmonic Nanoparticles for Cancer Therapeutics". IJP International Journal of Pharmaceutics, 524*(1-2), 16-29.

Research, N. W. (2006). *"Solo PIV Nd:YAG Laser Systems"*. In.

Rodward Hewlin Jr., A. Ciero., John Kizito. (2019). *"Development of a Two-Way Coupled Eulerian–Lagrangian Computational Magnetic Nanoparticle Targeting Model for Pulsatile Flow in a Patient-Specific Diseased Left Carotid Bifurcation Artery". Biomedical Engineering Society*.

Shintani, Y., Lino, K., Yamamoto, Y. et al. (2018). *"Analysis of Computational Fluid Dynamics and Particle Image Velocimetry Models of Distal-End Side-to-Side and End-to-Side Anastomoses for Coronary Artery Bypass Grafting in Pulsatile Flow". Circulation Journal, 82*(1), 110-117.

Shit, G. C., & Majee, S. (2015). *"Pulsatile Flow of Blood and Heat Transfer with Variable Viscosity under Magnetic and Vibration Environment". MAGMA Journal of Magnetism and Magnetic Materials, 388*, 106-115.

Shubayev, V. I., Pisanic, T.R., and Jin, S. (2009). *"Magnetic Nanoparticles for Theragnostics". Adv Drug Deliv Rev, 61*(467-477).

Song, M., Choi, H., Hyun, J., et al. (2014). *"Matching-Index-of-Refraction of Transparent 3D Printing Models for Flow Visualization". Nuclear Engineering and Design, 284*, 185-191.

Stoiber, M., Schloglhofer, T., Aigner, P., et al. (2013). *"An Alternative Method to Create Highly Transparent Hollow Models for Flow Visualization". International Journal of Artificial Organs, 36*(2), 131-134.

Sui, B., Gao, P., Lin, Y., Gao, B., Liu, L., and An, J. (2008). *"Assessment of Wall Shear Stress in the Common Carotid Artery of Healthy Subjects Using 3.0-tesla Magnetic Resonance". Acta. Radiol., 49*(4), 442-449.

Tehrani, M. D., Kim, M. O., & Yoon, J. (2014). *"A Novel Electromagnetic Actuation System for Magnetic Nanoparticle Guidance in Blood Vessels". IEEE Transactions on Magnetics, 50*(7).

Tuoi Vo, W. L., Adam Peddle, Martin Meere. (2017). *"Modelling Chemistry and Biology after Implantation of a Drug-Eluting Stent. Part I: Drug Transport". Mathematical Biosciences & Engineering*.

Vetel, J., Garon, A., and Pelletier, S. (2009). *"Lagrangian Coherent Structures in the Human Carotid Artery Bifurcation". Exp. Fluids, 46*(6), 1067-1079.

W. Thielicke, E. J. S. (2014). *"PIVlab: Time-Resolved Digital Particle Image Velocimetry Tool for MATLAB". Open Research Software*.

Xiao, L., Beibei, S., Huilin, Z., et. al. (2018). *"Retrospective Study of Hemodynamic Changes Before and After Carotid Stenosis Formation by Vessel Surface Repairing". Nature, 5493*, 1-8.

Yellen, B. B., Erb, R. M., Son, H. S., Hewlin, J. R., Shang, H., & Lee, G. U. (2007). *"Traveling Wave Magnetophoresis for High Resolution Chip Based Separations". Lab on a Chip, 7*(12), 1681-1688.

Yip, R., Mongrain, A., Ranga, J., et al. (2004). *"Development of Anatomically Correct Mock-ups of the Aorta for PIV Investigations". Canadian Design Engineering Network CDEN Conference, Montreal Canada*.

Yousif, M., Holdsworth, D., and Poepping, T. (2009). *"Deriving a Blood-Mimicking Fluid for Particle Image Velocimetry in Sylgard-184 Vascular Models". Conf Proc IEEE Eng Med Viol Soc.*, 1412-1415.

Zhang, X. M., Le, T. A., & Yoon, J. (2017). *"Development of a Real Time Imaging-Based Guidance System of Magnetic Nanoparticles for Targeted Drug Delivery". Journal of Magnetism and Magnetic Materials, 427*, 345-351. doi:10.1016/j.jmmm.2016.10.056

APPENDIX A: Ansys Fluent Straight Pipe

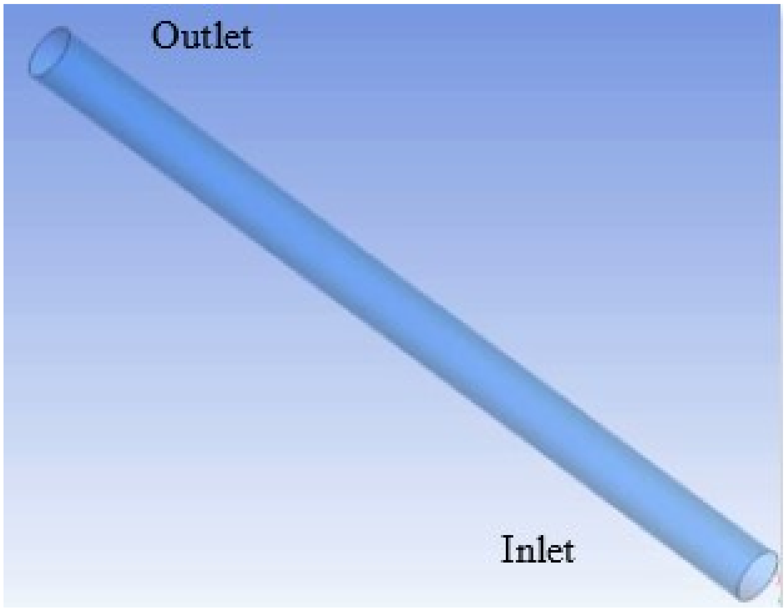

Figure A.1: Ansys Fluent Named Selections: Straight Pipe

APPENDIX B: Grid Independent Study for Ansys Fluent Bifurcating Artery

Table B.1: Grid Independent Study

Minimum Element Size	**Elements**	**Nodes**	**Avg WSS (Pa)**	**Avg Vel. (m/s)**	**Avg Vel. Inlet (m/s)**
5e-4 m	265029	83563	0.9972076	0.1502494	0.1307196
6e-4m	167191	55599	0.9585858	0.1452148	0.1307196
7e-4m	114885	39866	0.9482206	0.1413573	0.1307196
8e-4 m	80303	28791	0.9326587	0.1370787	0.1307196
10e-4m	47887	18182	0.9313318	0.1287911	0.1307196
12e-4m	30809	12086	0.9887976	0.1198822	0.1307196
14e-4m	21966	8964	1.01949	0.1146436	0.1307196

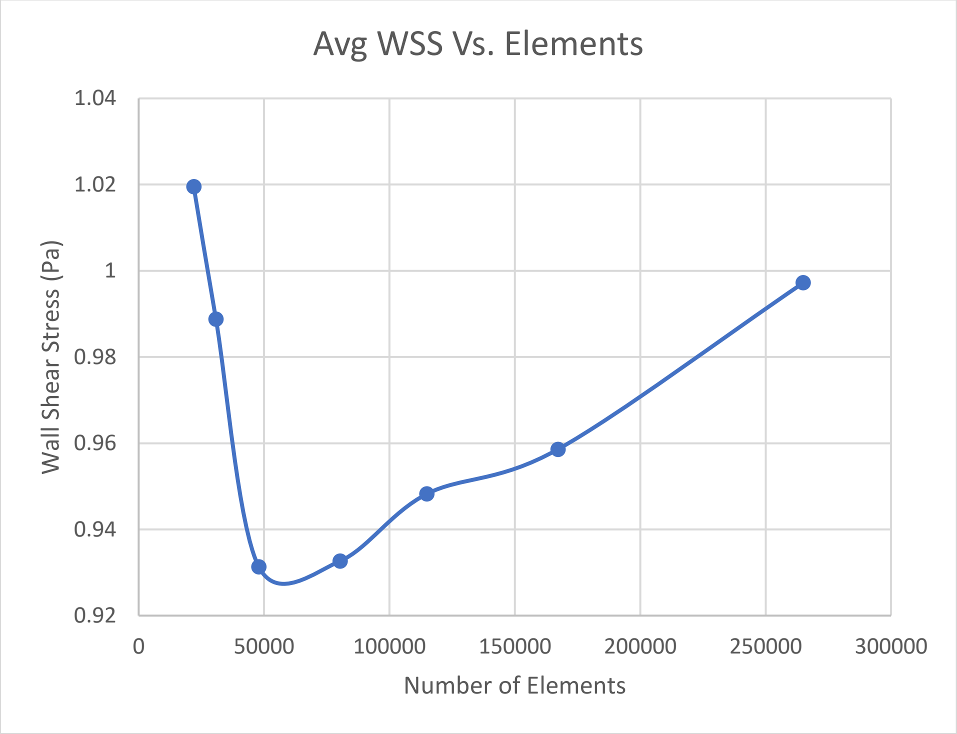

Figure B.1: Average Wall Shear Stress Vs. Number of Elements

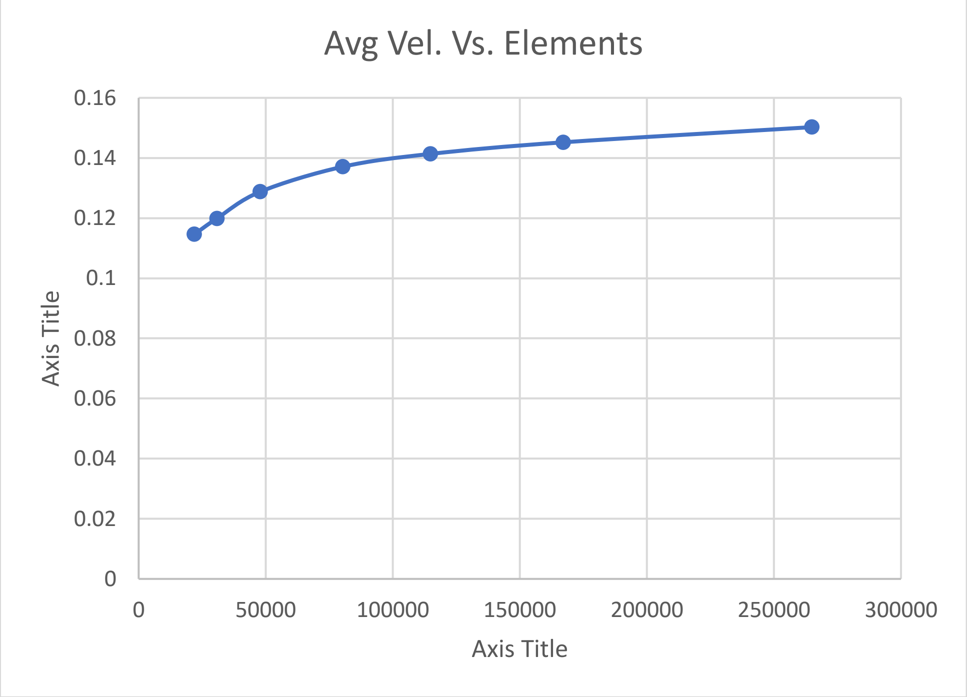

Figure B.2: Average Velocity Vs. Number of Elements

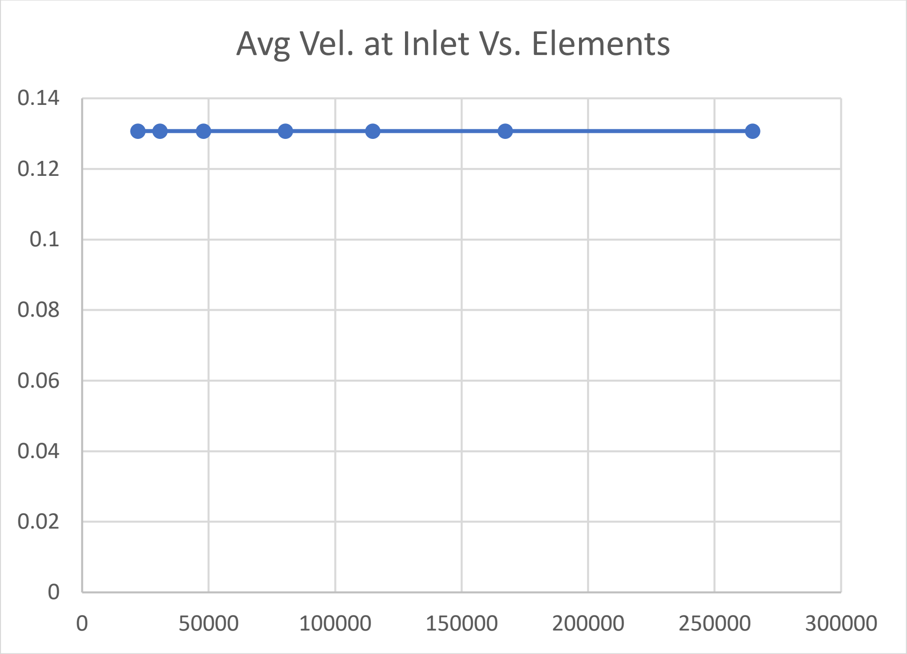

Figure B.3: Average Velocity at Inlet Vs. Number of Elements

APPENDIX C: Compliant Arterial Model

Future work should also involve comparing the PIV results of the 3-D printed rigid arterial model to a compliant model of the same geometry under the same conditions, as shown in *Figure C.1*.

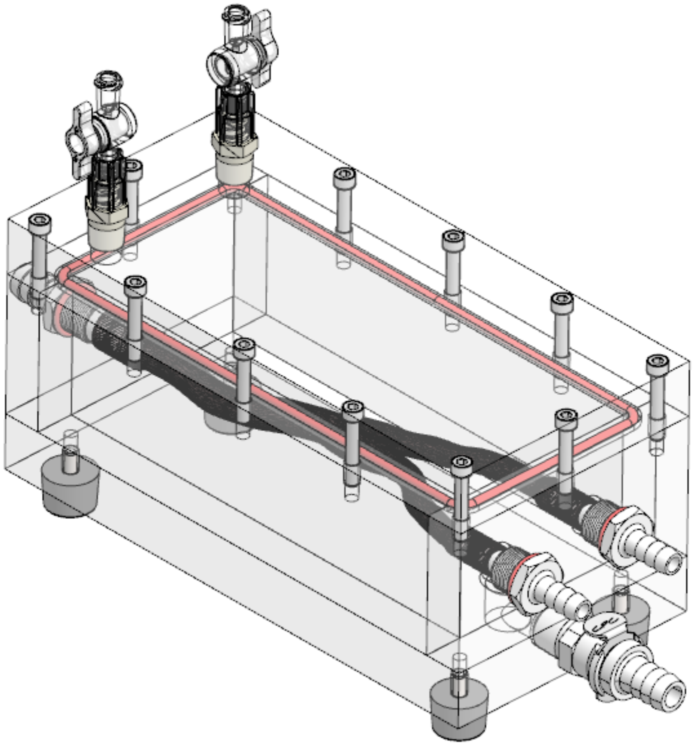

Figure C.1: Compliant Arterial Model

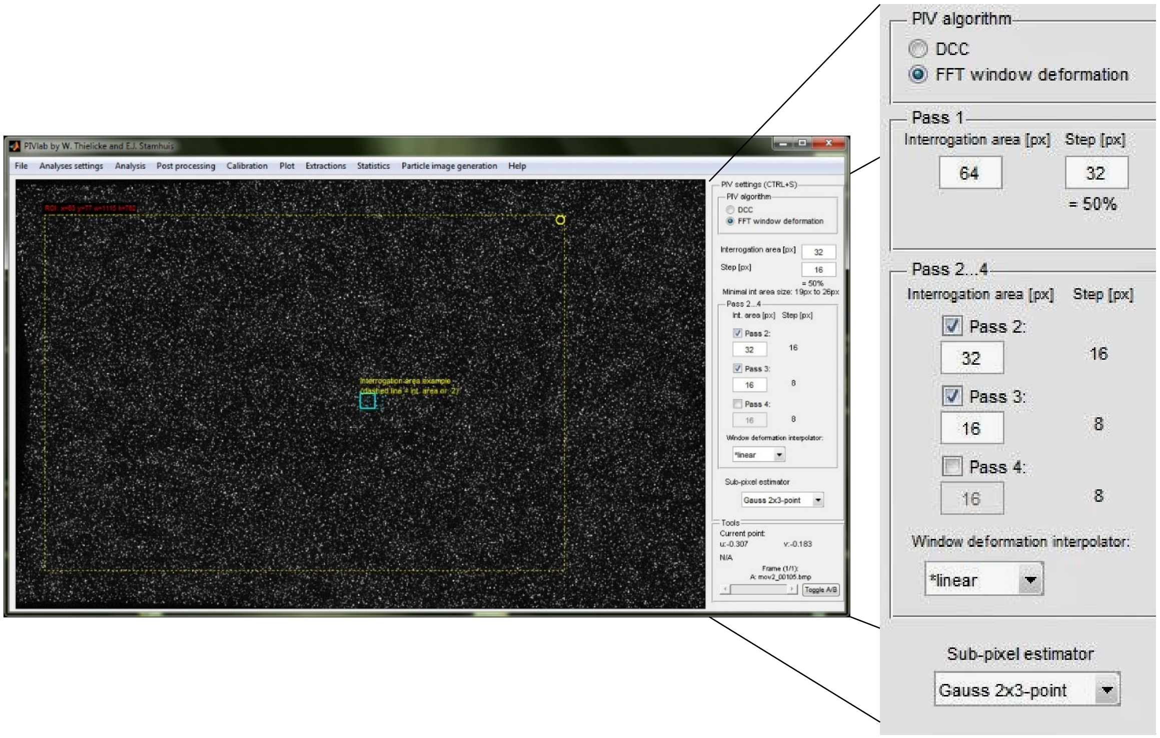

PIV algorithm
○ DCC
● FFT window deformation

Pass 1
Interrogation area [px]: 64
Step [px]: 32
= 50%

Pass 2...4

Interrogation area [px]	Step [px]
☑ Pass 2: 32	16
☑ Pass 3: 16	8
☐ Pass 4: 16	8

Window deformation interpolator: *linear

Sub-pixel estimator: Gauss 2x3-point

Figure D.1: PIVlab Example, obtained from (W. Thielicke, 2014)

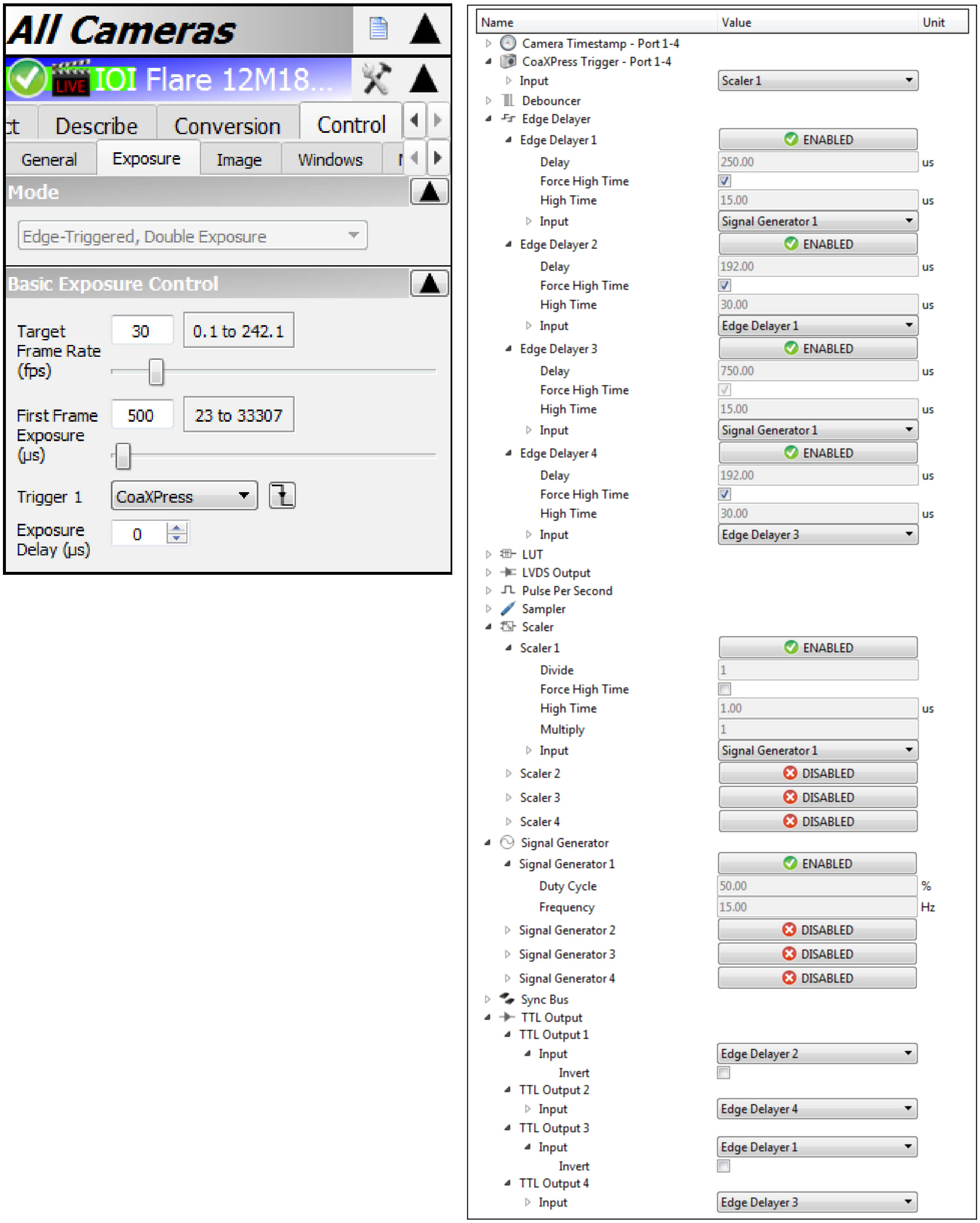

Mode

Edge-Triggered, Double Exposure

Basic Exposure Control

Target Frame Rate (fps): 30 (0.1 to 242.1)

First Frame Exposure (µs): 500 (23 to 33307)

Trigger 1: CoaXPress

Exposure Delay (µs): 0

Name	Value	Unit
Camera Timestamp - Port 1-4		
CoaXPress Trigger - Port 1-4		
Input	Scaler 1	
Debouncer		
Edge Delayer		
Edge Delayer 1	ENABLED	
Delay	250.00	us
Force High Time	☑	
High Time	15.00	us
Input	Signal Generator 1	
Edge Delayer 2	ENABLED	
Delay	192.00	us
Force High Time	☑	
High Time	30.00	us
Input	Edge Delayer 1	
Edge Delayer 3	ENABLED	
Delay	750.00	us
Force High Time	☑	
High Time	15.00	us
Input	Signal Generator 1	
Edge Delayer 4	ENABLED	
Delay	192.00	us
Force High Time	☑	
High Time	30.00	us
Input	Edge Delayer 3	
LUT		
LVDS Output		
Pulse Per Second		
Sampler		
Scaler		
Scaler 1	ENABLED	
Divide	1	
Force High Time	☐	
High Time	1.00	us
Multiply	1	
Input	Signal Generator 1	
Scaler 2	DISABLED	
Scaler 3	DISABLED	
Scaler 4	DISABLED	
Signal Generator		
Signal Generator 1	ENABLED	
Duty Cycle	50.00	%
Frequency	15.00	Hz
Signal Generator 2	DISABLED	
Signal Generator 3	DISABLED	
Signal Generator 4	DISABLED	
Sync Bus		
TTL Output		
TTL Output 1		
Input	Edge Delayer 2	
Invert	☐	
TTL Output 2		
Input	Edge Delayer 4	
TTL Output 3		
Input	Edge Delayer 1	
Invert	☐	
TTL Output 4		
Input	Edge Delayer 3	

Figure D.2: Frame Straddling Parameters